

Supporting Information

Conformal Monolayer Contacts with Lossless Interfaces for Perovskite Single Junction and Monolithic Tandem Solar Cells

Amran Al-Ashouri^{1*}, Artiom Magomedov^{2*}, Marcel Roß¹, Marko Jošt¹, Martynas Talaikis³, Ganna Chistiakova⁴, Tobias Bertram⁵, José A. Márquez⁵, Eike Köhnen¹, Ernestas Kasparavičius², Sergiu Levenco⁶, Lidón Gil-Escrig¹, Charles J. Hages⁶, Rutger Schlatmann⁵, Bernd Rech⁴, Tadas Malinauskas², Thomas Unold⁶, Christian A. Kaufmann⁵, Lars Korte⁴, Gediminas Niaura³, Vytautas Getautis² and Steve Albrecht^{1,7*}

¹Young Investigator Group Perovskite Tandem Solar Cells, Helmholtz-Zentrum Berlin, Kekuléstraße 5, 12489 Berlin, Germany

²Department of Organic Chemistry, Kaunas University of Technology, Radvilenu pl. 19, Kaunas LT-50254, Lithuania

³Department of Organic Chemistry, Center for Physical Sciences and Technology, Sauletekio Ave. 3, Vilnius LT-10257, Lithuania

⁴Institute for Silicon Photovoltaics, Helmholtz-Zentrum Berlin, Kekuléstraße 5, 12489 Berlin, Germany

⁵PVcomB, Helmholtz Zentrum Berlin für Materialien und Energie GmbH, 12489 Berlin, Germany

⁶Department of Structure and Dynamics of Energy Materials, Helmholtz-Zentrum-Berlin für Materialien und Energie GmbH, Hahn-Meitner Platz 1, 14109 Berlin, Germany

⁷Faculty of Electrical Engineering and Computer Science, Technical University Berlin, Marchstraße 23, 10587 Berlin, Germany

* Corresponding authors: amran.al-ashouri@helmholtz-berlin.de, steve.albrecht@helmholtz-berlin.de, artiom.magomedov@ktu.lt

Table of Contents

1. Experimental Part	2
Device preparation	2
Materials	3
Analysis Methods.....	3
Synthesis of the SAM molecules.....	6
2. Comparison of spin-coating, dipping and different SAM solution concentrations	10
3. Additional information to the RAIRS measurements	11
4. Additional device metrics.....	14
5. X-Ray Diffraction patterns and SEM pictures	16
6. Photocurrent Spectra to determine the Urbach Energy	17
7. Additional information to Photoelectron spectroscopy.....	18
Calculation of the dipole moment	22
8. Further PL measurements	23
Estimation of the interface recombination velocity	25
9. Certification Results	26
10. Additional results with the other perovskite absorbers	28
11. Additional results to the Perovskite/CIGSe Tandem	29

1. Experimental Part

Device preparation

Patterned indium tin oxide (ITO) glass substrates (25x25 mm, resistivity = $15 \Omega \text{ sq}^{-1}$, nominal ITO thickness = 150 nm, patterned by Automatic Research GmbH) were cleaned sequentially for 15 min with a 2% Mucosal solution in water (Schülke), water, Acetone, and Isopropanol at $\sim 40^\circ\text{C}$ in an ultrasonic bath. After that, directly before HTM deposition, the substrates were treated in an UV-ozone cleaner for 15 min. UV treatment seemed crucial for achieving a high reproducibility. All subsequent procedures were done in a nitrogen-filled glovebox (MBRAUN). For the PTAA devices, PTAA dissolved in anhydrous Toluene (both by Sigma Aldrich) was spin-coated from a 2 mg/ml solution in at 5000 rpm (5 s acceleration) for 30 s and heated on a hot plate at 100°C for 10 min.

SAM powders were dissolved in anhydrous Ethanol at a concentration of 1 mmol/l and put into an ultrasonic bath for 15 min ($30\text{--}40^\circ\text{C}$) before using. 2PACz powder (molar weight 335.3 g/mol) was stored in a nitrogen glovebox, MeO-PACz (275.24 g/mol) was stored in ambient air. If stored otherwise before dissolving, penalties in performance were observed. The SAMs were prepared either by spin-coating or dipping. When spin-coating, 100 μl of the solution was uniformly released onto the middle of the substrate, the lid was closed and after ~ 5 s resting, the spin-coating program (30 s at 3000 rpm) was started. Alternatively, a lower concentration of 0.1 mmol/l can be used if dropping the solution 2-3 times dynamically during the spinning program. After spin-coating, the substrates were heated at 100°C for 10 min. A washing step (with Ethanol) is possible but not necessary. For some perovskites, it might be beneficial to wash the substrates after heating, since it can change the contact angle of the perovskite (no significant performance differences were observed for all used perovskites in this work). SAMs by dipping were prepared by immersing the substrates into a 0.1 mmol/l solution for 2-12h, with subsequent heating at 100°C for 10 min. After heating, the dipped substrates were washed dynamically during a 4000 rpm, 30 s spin-coating program by dripping 100-200 μl of Ethanol 2-3 times onto them.

Triple-cation $\text{Cs}_{0.05}(\text{MA}_{0.17}\text{FA}_{0.83})_{0.95}\text{Pb}(\text{I}_{0.83}\text{Br}_{0.17})_3$ (CsMAFA) perovskite film was formed according to our previously reported procedure¹. 100 μl of the precursor was dripped onto the PTAA or SAM-covered substrates and the solution was spread with a pipette tip across the substrate before starting the spinning program (5s acceleration to 4000 rpm, 35s steady at 4000 rpm). On PTAA, 500 μl of Ethyl Acetate as the antisolvent was dripped onto the perovskite 25 s after starting the spin-coating program (closed spin-coater lid). On SAMs, either Ethyl Acetate, or, in later optimized stages, 200 μl of Chlorobenzene or Anisole² were used as the antisolvent (with open lid during the program), dripped 5-7 s before the end of the spinning program (with 3500 instead of 4000 rpm spinning speed). The SAMs are chemically robust and allow the use of more types of antisolvents than PTAA. Further, the perovskite was annealed at 100°C for 30-60 min.

Double cation $\text{MA}_5\text{FA}_{95}\text{Pb}(\text{I}_{95}\text{Br}_5)_3$ (MAFA) perovskite was prepared similarly to the CsMAFA perovskite, with respectively changed ratio of mixing the MAPbBr_3 and FAPbI_3 precursor solutions and 60 min annealing. The final perovskite solution was mixed just before spin-coating. Additionally, a 1.24 mol/l MACl solution in DMSO was mixed with the perovskite solution in a 5:95 volume ratio. The same spin-coating program as for CsMAFA was used, with dripping 300 μl Chlorobenzene 5s before the end of the program.

Single cation MAPbI_3 was prepared by direct co-evaporation using a CreaPhys “PEROvap” deposition tool integrated into an inert glovebox (MBraun). The system includes a cooling shield inside the chamber, whose temperature was set to -25°C for the entire process time. The rotation speed of the substrate holder was held constant at 10 rpm. Lead iodide and Methylammonium iodide were filled in two individual crucibles and the chamber was evacuated. At reaching a base pressure of $1\text{E-}6$ mbar the sources were heated to 240°C (PbI_2) and 150°C (MAI). Starting from this point the temperature was

slightly adjusted until a stable rate of 1.4 \AA s^{-1} (PbI₂) and 3.5 \AA s^{-1} (MAI) were obtained. The ratio was monitored using individual quartz crystal microbalances (QCM, Inficon) for each material.

After perovskite deposition, 23 nm C60 and 8 nm BCP were thermally evaporated in a MBRAUN ProVap 3G at a base pressure of $1\text{E-}6$ mbar with an evaporation rate of 0.1-0.18 \AA/s . For completing the device, 100 nm Cu or Ag was thermally evaporated through a shadow mask. The overlap of the substrate's ITO with the Cu stripe defines the active area of 0.16 cm^2 (cross-checked with an optical microscope).

Some devices, such as the one sent for certification, were encapsulated with a cover glass and a two-component self-curing epoxy glue (5-min epoxy, R&G Faserverbundwerkstoffe GmbH). After encapsulation, an antireflective coating (100 nm NaF) was thermally evaporated onto the glass substrates, which increased the short-circuit current density distinctly stronger for 2PACz and MeO-2PACz devices than for PTAA and V1036 devices.

When employing SnO₂ instead of BCP, we noticed better and more stable performance with MeO-2PACz than with 2PACz, possibly due to a faster hole-extraction with MeO-2PACz.

CIGSe/perovskite tandem solar cell

The CIGSe bottom cell was fabricated in a multi-step thermal evaporation on a glass substrate as described in the SI of our previous work³, with RbF surface treatment. The p-type back contact is made of sputtered Molybdenum. The recombination contact consists of 10 nm sputtered i-ZnO and 140 nm ZnO:Al (AZO). After completion, the surface was rinsed with Ethanol and treated with UV-Ozone for 15 min, before submersing the CIGSe bottom cell into a 0.1 mmol/l MeO-PACz/Ethanol solution overnight. Spin-coating a 1 mmol/l MeO-PACz solution once or a 0.1 mmol/l solution three times also yielded >20 %-efficient tandem cells. Subsequently, the bottom cell was heated at 100 °C for 10 min in a N₂-filled glovebox, before proceeding the CsMAFA perovskite processing on top as described above.

After perovskite annealing, 20 nm C60 was thermally evaporated and 20 nm of SnO₂ processed on top at a substrate temperature of 80 °C via atomic layer deposition (ALD, Arradiance GEMStar) to form a buffer layer for the indium zinc oxide (IZO) sputtering, as optimized in another work⁴. SnO₂ precursors were tetrakis(dimethylamino)tin(IV) (TDMASn) and water. The IZO top electrode was deposited by RF sputtering from a 10% wt ZnO and 90 % wt In₂O₃ target. For contacting the electrode, a 100 nm thick Ag frame was thermally evaporated through a shadow mask and 100 nm LiF as the anti-reflective coating. After device completion, the tandem cell was manually scribed around the Ag frame, since the AZO recombination and Molybdenum back contact were both processed on the full bottom cell area.

Materials

The molecules that form SAMs were synthesized (see next section). All other materials for the perovskite precursor and for evaporation were used as bought without further purification. Lead iodide and lead bromide were purchased from TCI (99.99%, trace metals basis) or Sigma Aldrich (99.999%, trace metals basis). FAI and MABr were purchased from Dyenamo (grade 99%), CsI from abcr GmbH (99.999%). Solvents (all anhydrous) DMF, DMSO and antisolvents ethyl acetate, chlorobenzene and anisole were from Sigma Aldrich, the SAM solvent ethanol was bought from VWR Chemicals. PTAA was by Sigma Aldrich.

Electron-selective contact and top electrode: C60 (99.99%) and BCP from Sigma Aldrich, Cu shots from Alfa Aesar.

For co-evaporated MAPbI₃, lead iodide by TCI and Methylammonium iodide by Lumtec were used.

Analysis Methods

Molar extinction coefficient

The SAM or PTAA powders were dissolved in Chlorobenzene at a concentration of 1 mmol/l. The absorption spectra were recorded from the solution in a cuvette in a PerkinElmer Lambda 35 spectrometer.

Infrared spectroscopy (RAIRS and FTIR)

Reflection absorption infrared spectroscopy (RAIRS) data were recorded using Vertex 80v (Bruker Inc., Leipzig, Germany) spectrometer equipped with liquid nitrogen cooled narrow-band MCT detector. Samples were placed onto a horizontal accessory in evacuated (~2 mbar) spectrometer chamber. The bare ITO substrate was used as a reference. The spectra were taken with p-polarized incident light after incubation of the samples in vacuum for 180 s. Spectral resolution was set to 4 cm^{-1} , aperture to 4 mm, and spectra were acquired by averaging 256 scans. The spectra were taken in three steps: First, samples were measured as received. Next, they were rinsed with ethanol and incubated in chlorobenzene for 10 min in order to remove any possible multilayers and measured again. Lastly, measurements were repeated after one month to identify any changes occurring due a degradation of the samples (see fig. S6).

Fourier transform infrared (FTIR) spectra of bulk materials were taken from KBr pellet-pressed V1036 (**V1036**), MeO-2PACz (**V1193**) and 2PACz (**V1194**) samples, using an Alpha (Bruker Inc., Leipzig, Germany) spectrometer equipped with a DLATGS detector in transmission mode. The resolution was set to 4 cm^{-1} . Geometry optimization and frequency calculations were performed using Gaussian 09W software with Becke three parameter functional, B3LYP, and def2-SVP basis set for V1036 and B3LYP functional with 6-311++g(2d,p) basis set for MeO-2PACz and 2PACz compounds. The scaling factor was applied for the theoretical results as described in a previous publication⁵.

Solar cell characterization

Current-voltage (J-V) characteristics under 1 sun equivalent illumination were recorded using a Wavelabs Sinus-70 LED class AAA sun simulator in air, calibrated with a filtered KG3 Silicon reference solar cell certified by Fraunhofer ISE. J-V scans were performed as 2-point measurements with a Keithley 2400 SMU (4-point measurement with Keithley 2600 for the tandem cell), controlled by a measurement control program written in LabView. The single junctions were not masked during measurement (due to small differences between J_{SC} from integrated EQE and J-V). The voltage values are swept in 20 mV steps with an integration time of 40 ms per point and settling time of 20-40 ms after voltage application (maximum voltage sweep speed of 250 mV/s). EQE spectra were recorded with an Oriel Instruments QEPVSI-b system with a Newport 300 W xenon arc lamp, controlled by TracQ-Basic software. The white light filtered into monochromatic light by a Newport Cornerstone 260 monochromator with a 10 nm increment and chopped into a frequency of 78 Hz before being conducted to the solar cell surface via optical fibers. The system is calibrated using a Si reference cell with known spectral response before every measurement. The electrical response of the device under test is measured with a Stanford Research SR830 Lock-In amplifier (time constant of 0.3 s) and evaluated in TracQ. The typical short-circuit current mismatch between integrated external quantum efficiency (EQE) times AM1.5G irradiance and values from J-V scans is around 1%. For the Urbach energy estimation, the monochromator step size is reduced to 2 nm and Lock-In integration time increased to 1 s per increment.

The temperature during continuous MPP tracking was measured with a thermocouple attached to the samples's glass surface.

A spectral mismatch M^6 for the used solar simulator was calculated with typical CsMAFA and MAFA EQE spectra, the spectral response of the calibrated reference cell and the spectrum of the solar simulator. The small deviations from 1 ($M = 0.997$ for CsMAFA and 1.005 for MAFA) are within the measurement error margins during J-V characterizations, thus the measured J_{SC} values were not corrected by $1/M$.

No pre-conditioning protocols were applied. For some cells, we observed a slight rising trend in V_{OC} upon multiple J-V scans (or some minutes of light-soaking until thermodynamic stabilization). Typically, the PCE value of the PSCs saturates at higher values a few days after perovskite processing.

Photoelectron spectroscopy

XPS measurements were conducted with a non-monochromated Mg K α excitation source and a ScientaOmicron Argus CU electron analyzer in the Energy Materials In-Situ Laboratory (EMIL) of HZB. Core level peak fitting was performed with the free software fityk⁷. The number of Voigt peaks was determined by fitting all three datasets simultaneously with coupled width and shape parameters and increasing the number of peaks until the residuum was in the order of the background noise of the data. A linear background was included into the fit.

UPS measurements were conducted with the same equipment employing He I (21.22 eV) excitation. For measuring the secondary electron cutoff, a 10 V bias was applied to the substrate. The valence band onset was determined by the leading edge extrapolation method (see fig. S15).

The ITO substrates were prepared in the same manner as for the solar cells, in order to accurately reflect device-relevant ITO modification. The high V_{OC} values and low leakage currents obtained with the SAM-based PSCs, the constant PCE in dependence of the used solution concentration (Fig. S3) and the similarity in RAIRS of SAMs prepared by spin-coating vs. dipping ascertains that the studied SAMs are closely packed and that saturation of coverage is fulfilled. After preparation of the glass/ITO substrates in a nitrogen-filled glovebox, they were quickly transferred into the ultra-high vacuum UPS system without exposure to ambient air.

Absolute and transient photoluminescence

Time-resolved photoluminescence (trPL) measurements were carried out in a home-built setup using excitation at a 660 nm wavelength from a pulsed supercontinuum laser light source (SuperK) with a spot size of 25-35 μm in diameter. The repetition rate was set to 304 kHz and the sample's PL emission was collected panchromatically through a photomultiplier. Utilizing a time-correlated single photon counting technique (TCSPC), the PL decay was recorded with a time resolution of approximately 4 ns. The excitation power was varied with a linear ND filter, tracked with a power meter and chosen as follows, for injecting approximately the amount of charge carriers that is relevant for device operation under 1-sun conditions: If at a 1-sun equivalent excess charge-carrier density Δn the PL decay is dominated by monomolecular recombination, the recombination rate R can be approximated by $\Delta n/\tau$, where τ is the monomolecular recombination-limited PL lifetime. At quasi steady state, the generation rate G equals R . Thus, G is roughly the photon flux per penetration depth (approximated by the film thickness ~ 500 nm) divided by the steady-state PL lifetime (we assume 500 ns). This G is compared to the expected G under 1-sun equivalent excitation for an absorber with 1.63 eV band gap, which is given by the respective integration of the AM1.5G irradiance spectrum ($1.5\text{E}+21 \text{ m}^{-2} \text{ s}^{-1}$). Under these estimations, a fluence of ca. 10-30 nJ/cm^2 of pulsed excitation should create a 1-sun equivalent quasi-steady-state situation. The samples were excited on the perovskite side.

Absolute photoluminescence spectra and hyperspectral images were recorded with a custom setup described in another work⁸. Excitation was performed with two 450 nm LEDs, calibrated to ~ 1 sun equivalent fluence and PL emission was collected with a CCD camera. Wavelength-selectivity of the PL emission was achieved by coupling a tunable liquid crystal filter in front of the camera. The setup was calibrated to absolute photon numbers with light sources of known fluences⁹, thus enabling to estimate the quasi fermi-level splitting from the generalized Planck law using the high-energy tail fit method.

XRD

X-ray diffraction patterns (only in SI) were recorded at room temperature using a Bruker D8 diffractometer in Bragg-Brentano geometry. For all measurements the Cu radiation from an X-ray tube operated at 40 mA and 40 kV acceleration voltage was used.

Synthesis of the SAM molecules

In brief, alkylation with dibromoethane of the respective carbazole derivatives was performed (compounds **1** and **2**), followed by an introduction of phosphonic acid ester groups via an Arbuzov reaction to yield the intermediate materials **3** and **4**. Finally, cleavage of the ethyl groups was performed with bromotrimethylsilane to produce the final products **2PACz** and **MeO-2PACz**. Further details are presented in the following

Chemicals, unless stated otherwise, were purchased from Sigma-Aldrich or TCI Europe and used as received without further purification. The ^1H and ^{13}C NMR spectra were taken on Bruker Avance III (400 MHz) spectrometer at RT. All the data are given as chemical shifts in δ (ppm). The course of the reactions products was monitored by TLC on ALUGRAM SIL G/UV254 plates and developed with UV light. Silica gel (grade 9385, 230–400 mesh, 60 Å, Aldrich) was used for column chromatography. Elemental analysis was performed with an Exeter Analytical CE-440 elemental analyzer, Model 440 C/H/N/. Electrothermal MELTEMP capillary melting point apparatus was used for determination of melting points.

UV/Vis spectra were recorded on a PerkinElmer Lambda 35 spectrometer.

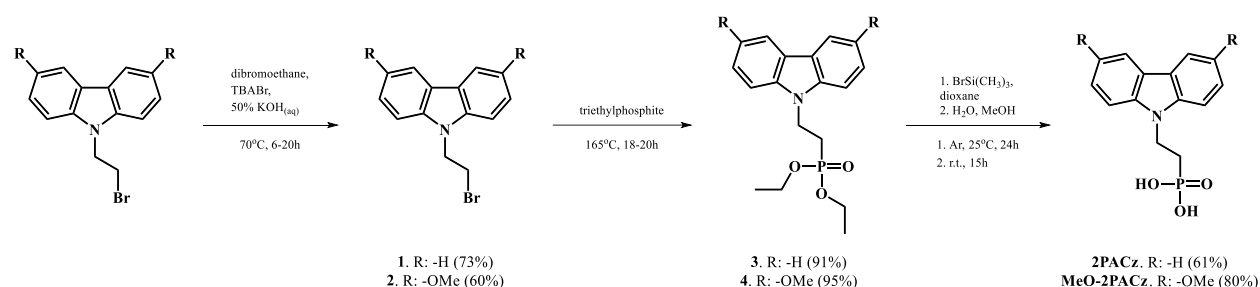
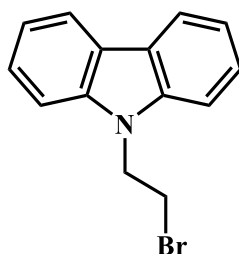


Figure S1 Synthesis scheme of the phosphonic acid functionalized carbazole derivatives **2PACz** and **MeO-2PACz**.

2PACz synthesis



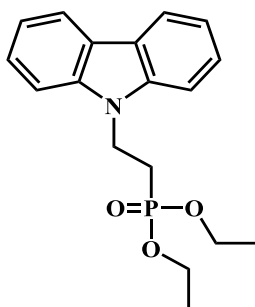
9-(2-bromoethyl)-9H-carbazole (**1**)

9H-carbazole (2 g, 12 mmol) was dissolved in 1,2-dibromoethane (20 ml), and tetrabutylammonium bromide (0.08 g, 0.25 mmol) with 50% KOH aqueous solution (7.2 ml) were added subsequently. Reaction was stirred at 70°C for 6 h (TLC, acetone:n-hexane, 3:22, v:v). After completion of the reaction, extraction was done with ethyl acetate. The organic layer was dried over anhydrous Na₂SO₄ and the solvent was distilled off under reduced pressure. The crude product was directly used for the further synthesis. 2.4 g (73 %) of white crystalline material was isolated— compound **1**.

Anal. calcd for C₁₄H₁₂NBr, %: C 61.33; H 4.41; N 5.11; found, %: C 61.39; H 4.37; N 5.03.

^1H NMR (400 MHz, CDCl₃) δ 8.08 (d, J = 7.7 Hz, 2H), 7.51 – 7.36 (m, 4H), 7.29-7.20 (m, 2H), 4.66 (t, J = 7.5 Hz, 2H), 3.64 (t, J = 7.5 Hz, 2H).

^{13}C NMR (101 MHz, CDCl₃) δ 140.05, 126.07, 123.25, 120.66, 119.70, 108.55, 44.77, 28.23.



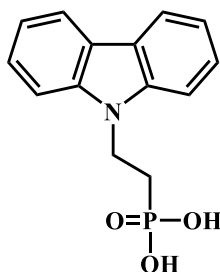
diethyl [2-(9*H*-carbazol-9-yl)ethyl]phosphonate (**3**)

Compound **1** (1.14 g, 4.16 mmol) was dissolved in triethylphosphite (14 ml) and the reaction mixture was heated at reflux for 20 h. After reaction completion (TLC, acetone:*n*-hexane, 7:18, v:v) the solvent was distilled off under reduced pressure. The crude product was purified by column chromatography using *n*-hexane as eluent, with the gradual change of the eluent to acetone:*n*-hexane, 1:4, v:v, to give 1.25 g (91%) of clear liquid – compound **3**.

Anal. calculated for C₁₈H₂₂NO₃P, %: C 65.25; H 6.69; N 4.23; found, %: C 64.99; H 6.60; N 4.16.

¹H NMR (400 MHz, DMSO-*d*₆) δ 8.15 (dd, *J* = 7.9, 1.9 Hz, 2H), 7.58 (d, *J* = 8.2 Hz, 2H), 7.52 – 7.43 (m, 2H), 7.26 – 7.17 (m, 2H), 4.65 – 4.54 (m, 2H), 3.94 – 3.85 (m, 4H), 2.35 – 2.21 (m, 2H), 1.23 (t, *J* = 7.0 Hz, 16H).

¹³C NMR (101 MHz, DMSO) δ 139.49, 125.71, 122.34, 120.26, 118.96, 109.20, 61.22, 61.16, 36.59, 24.95, 23.59, 15.97.



[2-(9*H*-carbazol-9-yl)ethyl]phosphonic acid (**2PACz**)

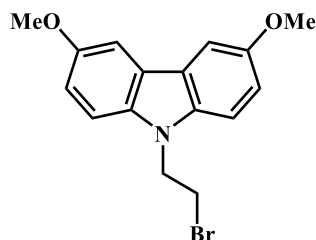
Compound **3** (1 g, 3.02 mmol) was dissolved in dry 1,4-dioxane (30 ml) under argon. Afterwards, bromotrimethylsilane (4 ml) was added dropwise. Reaction was kept for 24 h at 25 °C under argon atmosphere. Afterwards solvent was distilled off under reduced pressure, solid residue was dissolved in methanol (30 ml) and distilled water was added dropwise (150 ml), until solution became opaque, and was stirred for 24 h. The solution was concentrated under vacuum and the product was filtered off and washed with water to give 0.510 g (61 %) of pale-blue solid – **2PACz**.

Anal. calculated for C₁₄H₁₄NO₃P, %: C 61.09; H 5.13; N 5.09, found, %: C 60.64; H 5.22; N 5.02.

¹H NMR (400 MHz, DMSO-*d*₆) δ 8.15 (d, *J* = 7.8 Hz, 2H), 7.54 (d, *J* = 8.2 Hz, 2H), 7.51 – 7.42 (m, 2H), 7.21 (t, *J* = 7.4 Hz, 2H), 4.62 – 4.49 (m, 2H), 2.12 – 1.96 (m, 2H).

¹³C NMR (101 MHz, DMSO) δ 139.40, 125.85, 122.29, 120.41, 118.96, 108.93, 37.37, 27.94, 26.64.

MeO-2PACz synthesis



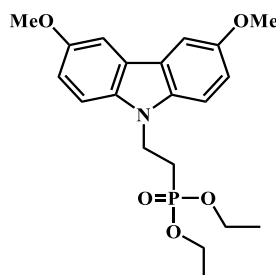
9-(2-bromoethyl)-3,6-dimethoxy-9H-carbazole (2)

3,6-dimethoxycarbazole (0.534 g, 2.35 mmol) was dissolved in 1,2-dibromoethane (8 ml), and tetrabutylammonium bromide (0.08 g, 0.25 mmol) with 50% KOH aqueous solution (6.9 ml) were added subsequently. Reaction was stirred at 70°C for 20 h (TLC, acetone:n-hexane, 3:22, v:v). After completion of the reaction, extraction was done with ethylacetate. The organic layer was dried over anhydrous Na₂SO₄ and the solvent was distilled off under reduced pressure. The crude product was purified by column chromatography using acetone:n-hexane, 1:49, v:v as eluent to give 0.352 g (60 %) of white crystalline material – compound **2**.

Anal. calcd for C₁₆H₁₆O₂NBr, %: C 57.50; H 4.83; N 4.19; found, %: C 57.39; H 4.86; N 4.15.

¹H NMR (400 MHz, CDCl₃) δ 7.51 (d, *J* = 2.5 Hz, 2H), 7.29 (d, *J* = 8.8 Hz, 2H), 7.10 (dd, *J* = 8.8, 2.5 Hz, 2H), 4.62 (t, *J* = 7.5 Hz, 2H), 3.93 (s, 6H), 3.62 (t, *J* = 7.5 Hz, 2H).

¹³C NMR (101 MHz, CDCl₃) δ 153.85, 135.65, 123.39, 115.30, 109.41, 103.45, 56.27, 45.07, 28.55.



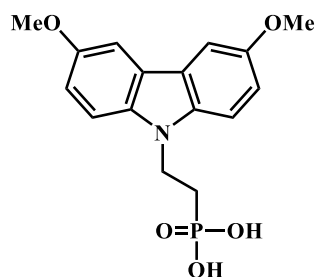
diethyl [2-(3,6-dimethoxy-9H-carbazol-9-yl)ethyl]phosphonate (4)

Compound **2** (0.316 g, 0.95 mmol) was dissolved in triethylphosphite (2.7 ml) and the reaction mixture was heated at reflux for 18 h. After reaction completion (TLC, acetone:n-hexane, 1:4, v:v) the solvent was distilled off under reduced pressure. The crude product was purified by column chromatography using acetone:n-hexane, 1:1, v:v as eluent to give 0.353 g (95%) of clear liquid – compound **4**.

Anal. calculated for C₂₀H₂₆NO₅P, %: C 61.37; H 6.70; N 3.58; found, %: C 61.32; H 6.73; N 3.55.

¹H NMR (400 MHz, CDCl₃) δ 7.52 (d, *J* = 2.5 Hz, 2H), 7.30 (d, *J* = 8.8 Hz, 2H), 7.10 (dd, *J* = 8.8, 2.5 Hz, 2H), 4.60 – 4.49 (m, 2H), 4.09 – 4.03 (m, 4H), 3.93 (s, 6H), 2.29 – 2.15 (m, 2H), 1.28 (t, *J* = 7.1 Hz, 6H).

¹³C NMR (101 MHz, CDCl₃) δ 153.67, 135.46, 123.37, 115.20, 109.49, 103.46, 62.02, 61.96, 56.28, 37.31, 26.15, 24.79, 16.56, 16.50.



[2-(3,6-dimethoxy-9H-carbazol-9-yl)ethyl]phosphonic acid (MeO-2PACz)

Compound **4** (0.335 g, 0.86 mmol) was dissolved in dry 1,4-dioxane (25 ml) under argon. Afterwards, bromotrimethylsilane (1.12 ml) was added dropwise. Reaction was kept for 24 h at 25°C under argon atmosphere. Afterwards solvent was distilled off under reduced pressure, solid residue was dissolved in methanol (15 ml) and distilled water was added dropwise (30 ml), until solution became opaque, and was stirred for 15 h. Product was filtered off and washed with water to give 0.230 g (80 %) of beige solid – **MeO-2PACz**.

Anal. calculated for C₁₆H₁₈NO₅P, %: C 57.32; H 5.41; N 4.18, found, %: C 57.19; H 5.53; N 4.11.

¹H NMR (400 MHz, MeOD) δ 7.57 (d, *J* = 2.5 Hz, 2H), 7.34 (d, *J* = 8.8 Hz, 2H), 7.05 (dd, *J* = 8.8, 2.5 Hz, 2H), 4.58 – 4.48 (m, 2H), 3.87 (s, 6H), 2.20 – 2.06 (m, 2H).

¹³C NMR (101 MHz, MeOD) δ 154.97, 136.71, 124.61, 116.03, 110.37, 104.29, 56.46, 38.47.

2. Comparison of spin-coating, dipping and different SAM solution concentrations

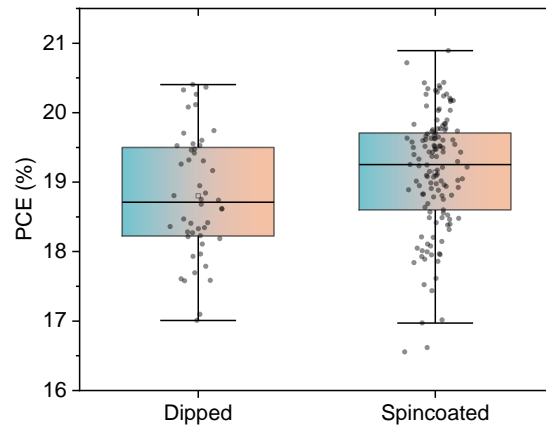


Figure S2 Statistical comparison between SAMs from spin-coating (no washing) and dipping (with subsequent washing), with triple cation perovskite absorber. The ITO substrates were either dipped into SAM solutions (0.1 mmol/l concentration in Ethanol, both MeO-2PACz and 2PACz are shown here) for several hours at room temperature with subsequent washing, or were prepared by spin-coating a 1 mmol/l SAM solution at 3000 rpm for 30s with subsequent heating at 100°C for 10 min. When spin-coating the SAM solution, subsequent washing of the substrates is optional and shows no PCE difference. Both preparation techniques yield similar efficiencies. The slightly higher average PCE obtained by SAMs from spin-coating is due to the fact that process optimization started with dipping and later stages predominantly spin-coating was used for single junction cells.

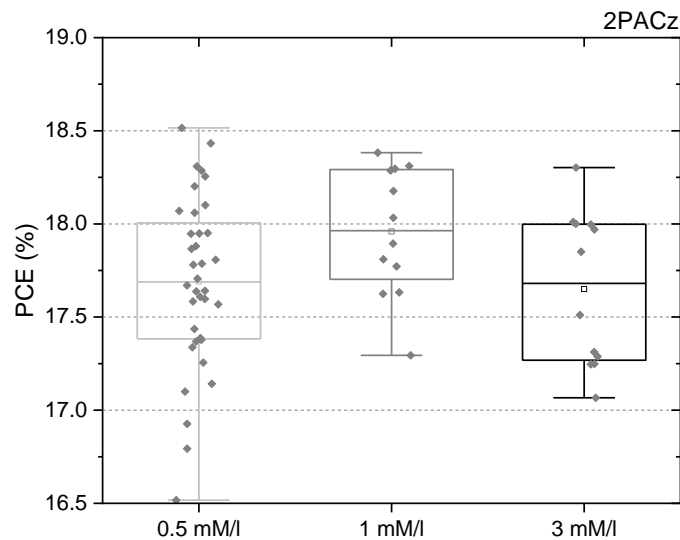


Figure S3 Power conversion efficiency of CsMAFA solar cells based on 2PACz, spin-coated from different concentrations in Ethanol.

3. Additional information to the RAIRS measurements

V1036: The high frequency feature at 1585 cm^{-1} was assigned to the asymmetric stretching vibrations of carbazole and p-methoxy-phenyl rings. 1484-cm^{-1} band was associated with carbazole ring stretching vibrations. Slightly lower frequency shoulder near $1441\text{--}1465\text{ cm}^{-1}$ has highest contribution from deformation vibrations of CH_3 groups. In-plane deformation vibrations of ring C–H bonds are visible at 1182 cm^{-1} . The broad band near 1010 cm^{-1} belongs to stretching vibration of phosphate group.^{10,11}

MeO-2PACz: Pair of well-defined bands of compound MeO-2PACz near 1164 and 1211 cm^{-1} are related with rings C–H in-plane deformation vibrations coupled with C–O stretching mode. Two carbazole ring stretching modes of compound 2PACz are visible at 1242 and 1347 cm^{-1} . Presence of phosphonic acid group can be recognized from the broad band at 1010 , 1021 , and 1017 cm^{-1} for V1036, MeO-2PACz, and 2PACz monolayers, respectively.

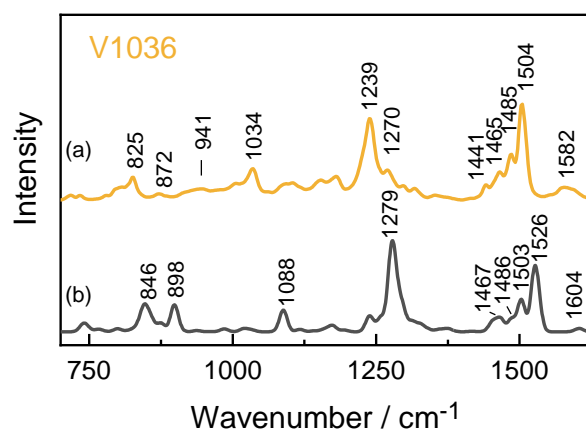


Figure S4 Comparison of FTIR spectrum of V1036 compound pressed into KBr pellet (a) and calculated spectrum at DEF2-SVP level of theory (b). The broad feature at 941 cm^{-1} for the bulk spectrum stems from P–OH species that are not present in monolayers.

Figure S4 shows the bulk spectrum of V1036 and the theoretical spectrum calculated by density functional theory (DFT), and figure S5 shows the same for MeO-2PACz and 2PACz. For V1036, the spectrum can be almost fully replicated by the calculation. For MeO-2PACz and 2PACz, prominent features can be replicated as well, although not all peaks expected by the DFT calculation can be found in the experimental spectra and vice versa, which we contribute to intermolecular interactions in the SAM, which are not present in the calculation that was conducted for a free-floating molecule in vacuum.

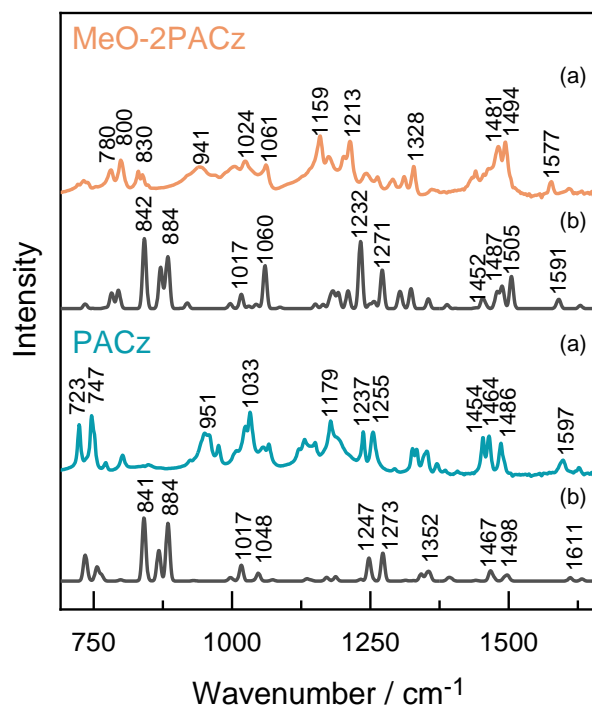


Figure S5 Comparison of FTIR spectrum of 2PACz and MeO-2PACz compounds pressed into KBr pellet (a) and calculated spectra at DEF2-SVP level of theory (b). The broad features at 941 cm^{-1} and 951 cm^{-1} stem from P-OH species¹⁰⁻¹³ that are not present in the monolayer spectra.

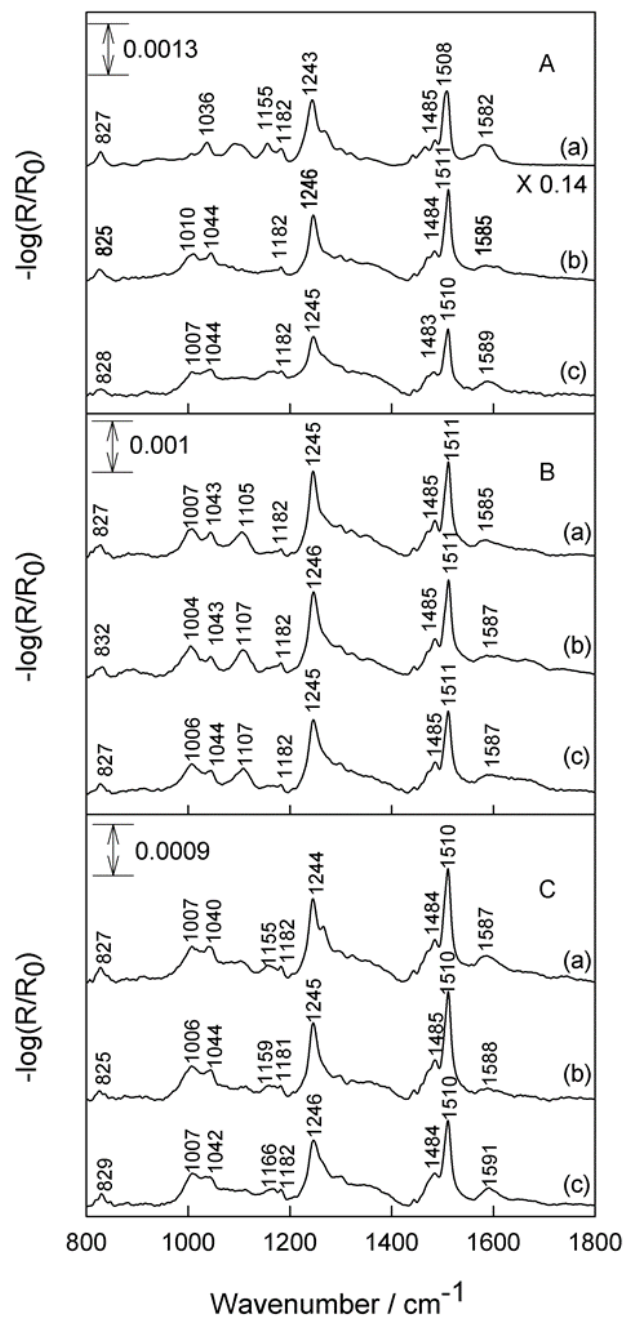


Figure S6 RAIRS spectra of different preparations of V1036 self-assembled monolayers on an ITO substrate. Spectra are shown of spin-coated (A) and formed from dipping (B, C, respectively) samples solutions before (a), after rinsing with ethanol and chlorobenzene (b) and after being kept in a lab environment for one month (c).

4. Additional device metrics

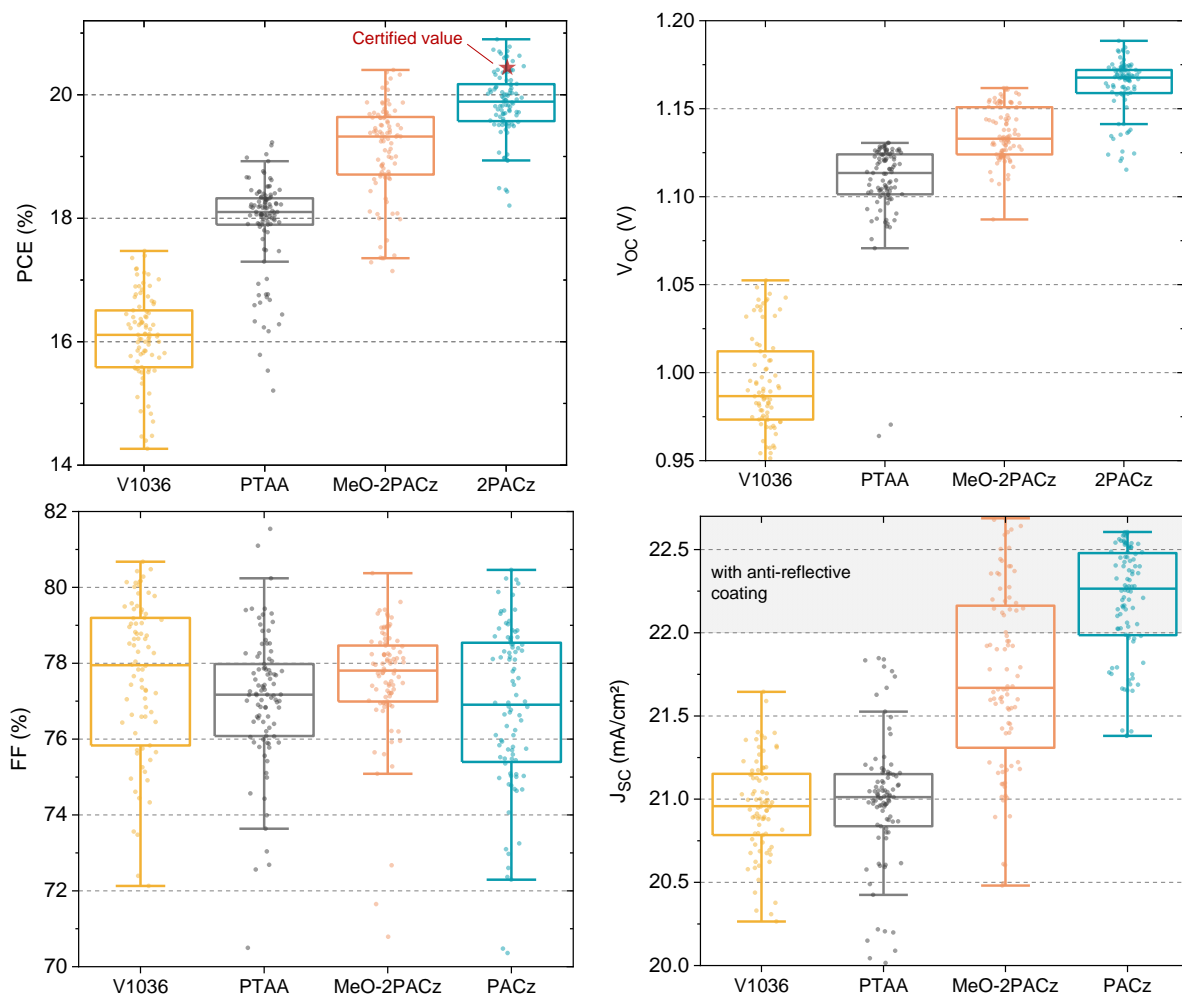


Figure S7 Solar cell device metrics for all investigated HTMs with CsMAFA “triple cation” perovskite absorber with 1.63 eV optical bandgap, on devices with area of 0.16 cm² (1:1 aspect ratio). The high J_{sc} values over 22 mA/cm² with both new SAMs are only achieved with a NaF antireflective (AR) coating. We notice that the AR coating is not as beneficial for PTAA-based devices, but adding 0.3 – 0.6 mA/cm² current density to 2PACz and MeO-2PACz devices. Note that, despite enabling a higher J_{sc} , the FF values of the (MeO-)2PACz devices are comparable to the ones of the PTAA devices, pointing to a higher extraction efficiency with (MeO-)2PACz.

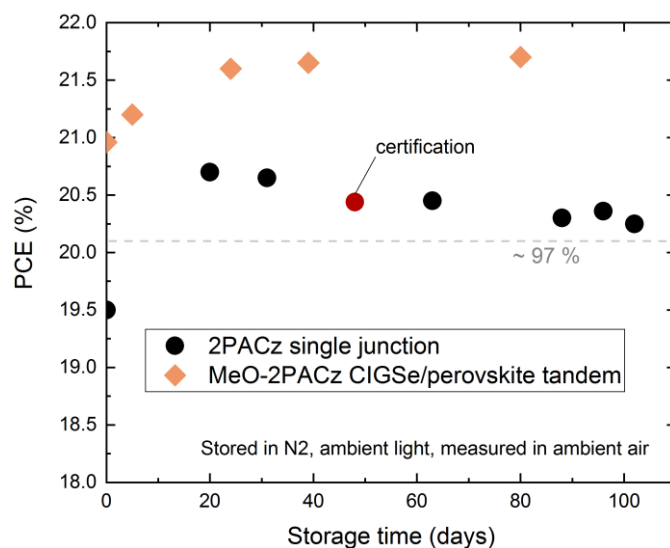


Figure S8 Initial stability assessment of SAM-based solar cells. The plot shows the time evolution of stabilized PCE of the single junction cell that was sent for certification. This cell was repeatedly handled and measured in ambient air (RH 30-60 %) and was stored in a nitrogen-filled glovebox in between the measurements. The orange points show the same for a representative CIGSe/perovskite tandem solar cell (same device stack as for the cell in the main text). The cell was measured in ambient air and was stored in nitrogen in between the measurement days. We expect that SAMs are suitable for the integration into PSC architectures that are specialized for high stability.

5. X-Ray Diffraction patterns and SEM pictures

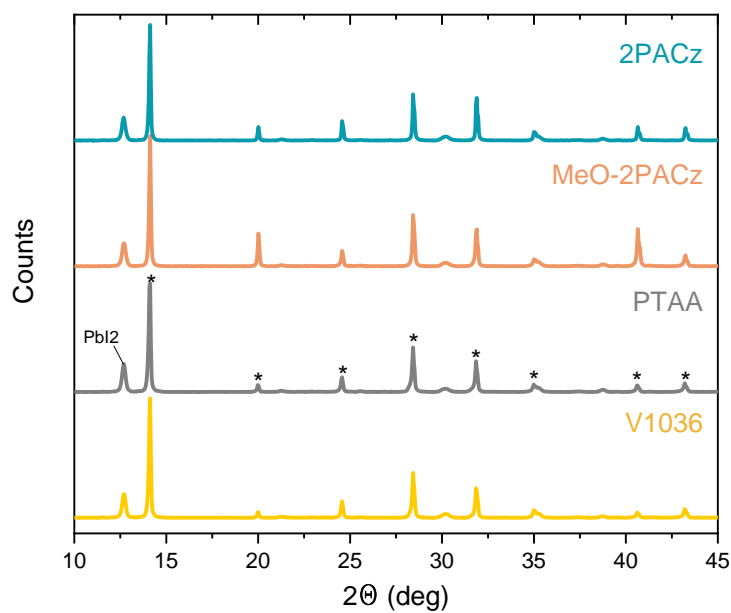


Figure S9 X-ray diffractograms of CsMAFA Perovskite films grown on the investigated HTMs (stack is glass/ITO/HTM/Perovskite). The stars on the PTAA case indicate the expected positions of perovskite crystal diffraction peaks.

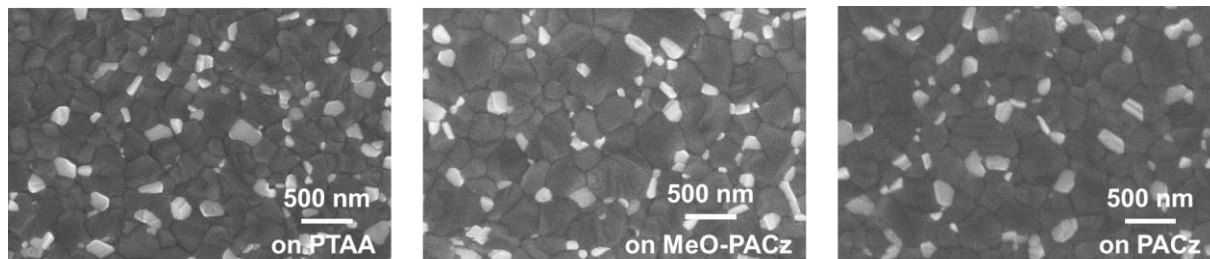


Figure S10 Scanning electron microscopy images of CsMAFA perovskite grown on PTAA, MeO-PACz and PACz. SEM pictures of the same perovskite on V1036 was previously published¹.

6. Photocurrent Spectra to determine the Urbach Energy

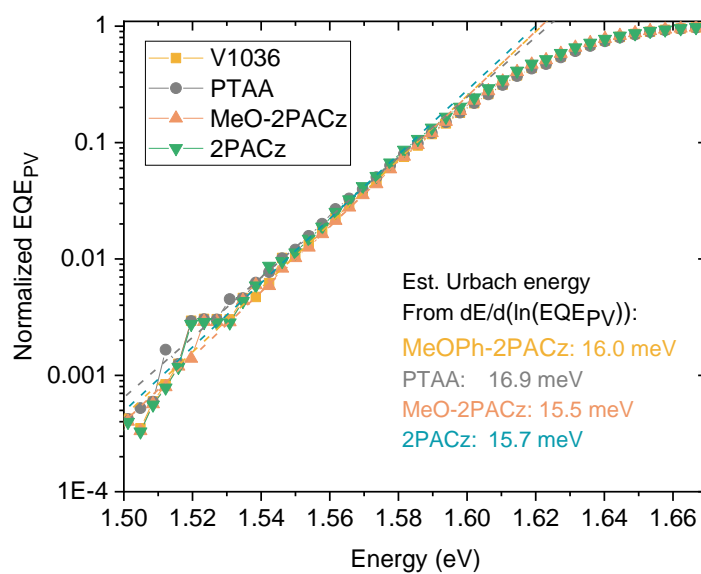


Figure S11 Normalized EQE of Perovskite solar cells based on the investigated HTMs, measured by a lock-in amplified current signal of the solar cell under modulated, monochromatic light (step size 2 nm & 1 second integration time). The slope in the “Urbach regime” gives an estimate of the energy of tail states (“Urbach energy”), which is likely to be overestimated by this method, but still gives a comparable value to the ones determined by a sophisticated full-fit.¹⁴ The kink at 1.52-1.53 eV might stem from the low spectral response of the reference cell used for calibration.

7. Additional information to Photoelectron spectroscopy

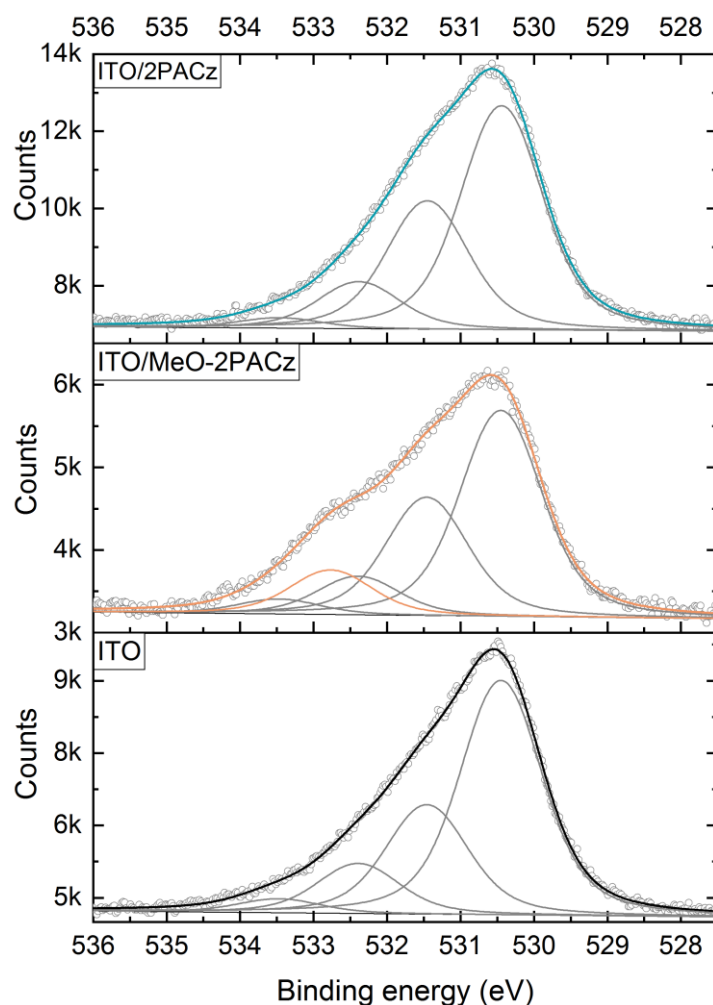


Figure S12 X-ray photoelectron spectroscopy (XPS) spectra in the O1s region of cleaned and O3-treated ITO (lower panel), ITO covered with MeO-2PACz (middle) and covered with 2PACz (top panel). After heating, the SAM-treated samples were washed with Ethanol. The number of necessary peaks for the fit was determined as for the C1s fitting in the main text (with linear background included into the fit). The peak shape parameters (Voigt curves) are the same for all shown peaks. For the (MeO-)2PACz fits, the relative distances between the peaks were locked to the same values as determined from the bare ITO fit, in order to unambiguously determine whether additional peaks are needed. Only the MeO-2PACz fit needed an additional peak (orange) that is here assigned to C-O-C species¹⁵, in conjunction with the C1s study of the main text. The largest peak at 530.5 eV is assigned to oxygen in In_2O_3 in both bulk and surface of the ITO¹⁶. In this case, a possible tin-oxygen bond coincides in binding energy with In-O bonds¹⁷. The second largest peak at 531.5 eV is assigned to metal hydroxide species¹⁵. The area ratio between this peak and the largest one is 0.47 for the bare ITO sample. Upon SAM treatment, this ratio rises to 0.57 for both MeO-2PACz and 2PACz, pointing either to an increased concentration of O-H groups¹⁸ on the surface or that less signal from the ITO bulk is collected. The remaining two peaks at higher binding energies might be assigned to other hydroxides and adventitious contaminants, like H_2O ^{15,16}. We assume that P-O species cannot be resolved here due to limited sensitivity and possible overlap with the contaminant peaks.

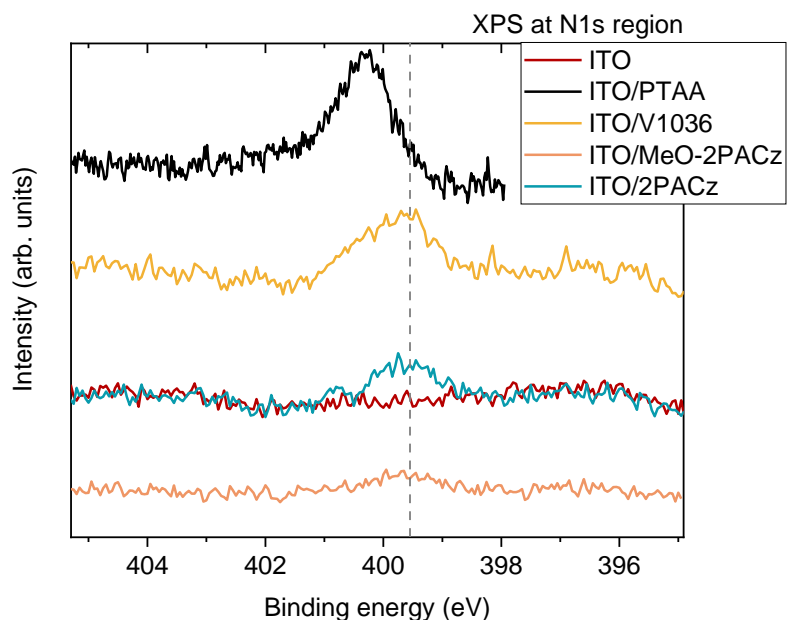


Figure S13 X-ray photoelectron spectroscopy on the studied substrates at the N1s region. Both MeO-2PACz and 2PACz share the same peak position, whereas V1036 shows a broader peak due to the presence of an additional N species in the diphenylamine group. A more detailed peak analysis would require a higher signal-to-noise ratio.

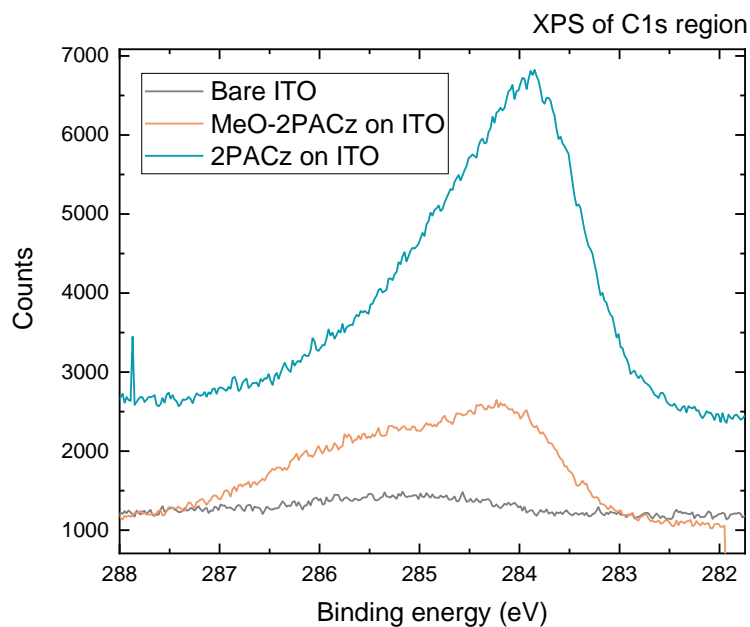


Figure S14 X-ray photoelectron spectroscopy at the C1s region of ITO glass, with and without SAM spin-coated on top (from 1 mmol/l solution, with subsequent heating to 100°C for 10 min). The residual small signal of the bare ITO sample is probably caused by adventitious carbon of the e. g. the sample storage boxes or glovebox.

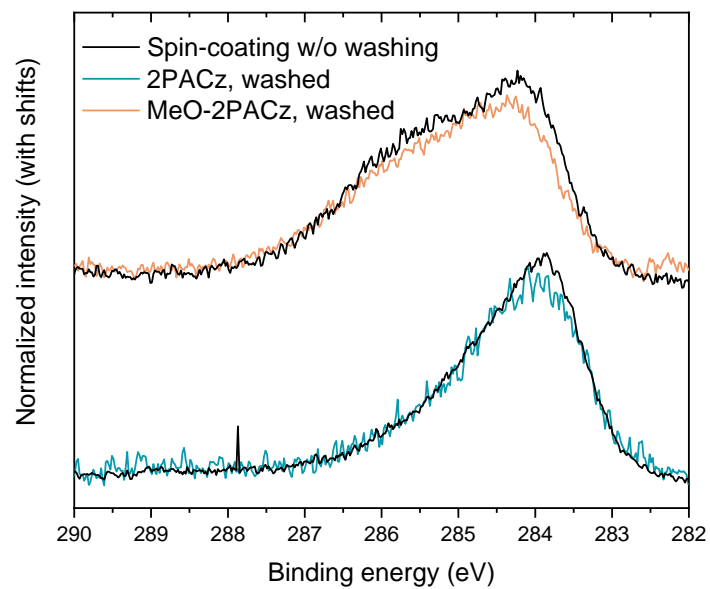


Figure S15 X-ray photoelectron spectroscopy at the C1s region for samples on which the SAM solution (1 mmol/l in Ethanol) was spin-coated (with subsequent heating to 100°C for 10 min), with and without washing the substrates subsequently.

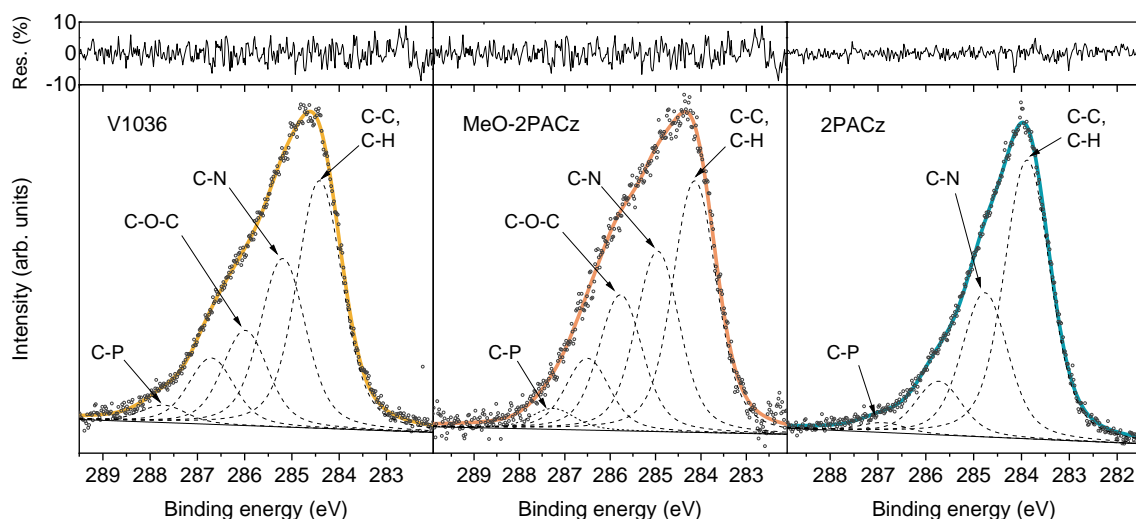


Figure S16 Same XPS measurement as in the main text, with the additional graph on top of each plot showing the relative residuum of each fit. The number of peaks was determined by fitting all three datasets globally with the same width and shape parameters and increasing the number of peaks until the residuum was in the order of the background noise of the data.

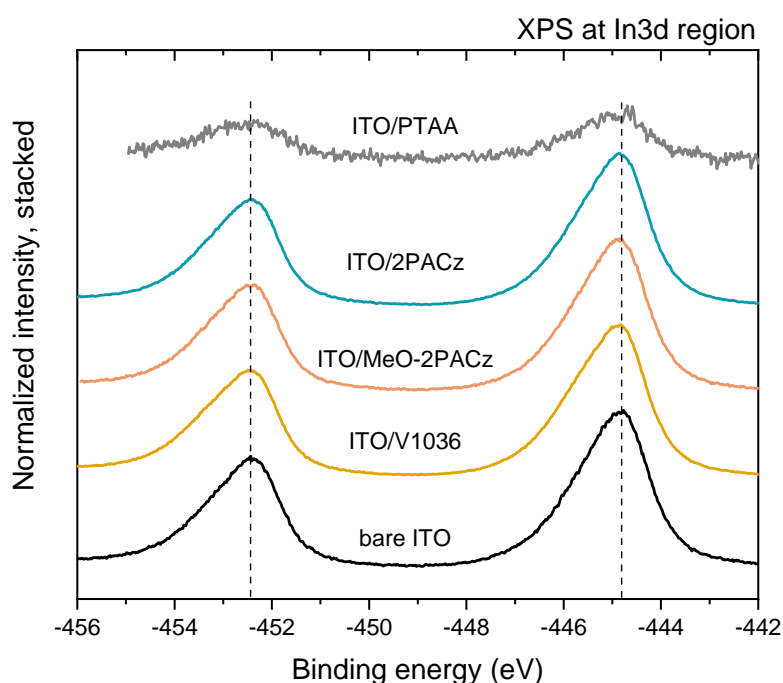


Figure S17 X-ray photoelectron spectra of the substrates on which UPS for the energy band edge diagram in fig. 4 of the main text (except for the perovskite values) has been conducted. The XPS measurement was recorded directly after the UPS measurement and shows the In peaks of the ITO substrate. All peaks are aligned, showing that no sample charging effects might have altered the energetic values.

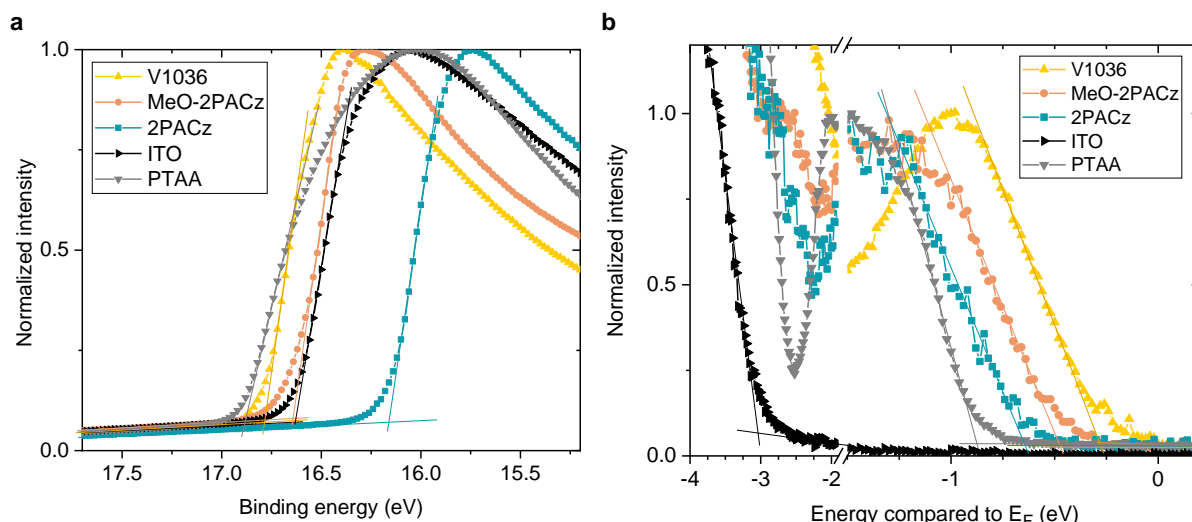


Figure S18 Ultra-violet photoelectron spectra (UPS) from which the work function (a) and valence band onset values (b) were extracted for the energy band edge diagram in fig. 4 of the main text (excitation energy is 21.22 eV). The excitation energy was 21.22 eV. After every UPS measurement, an XPS measurement was recorded to check for any charging effects of the substrates that could cause any shifts of the spectra (see comparisons of the substrates' In peaks in fig. S14).

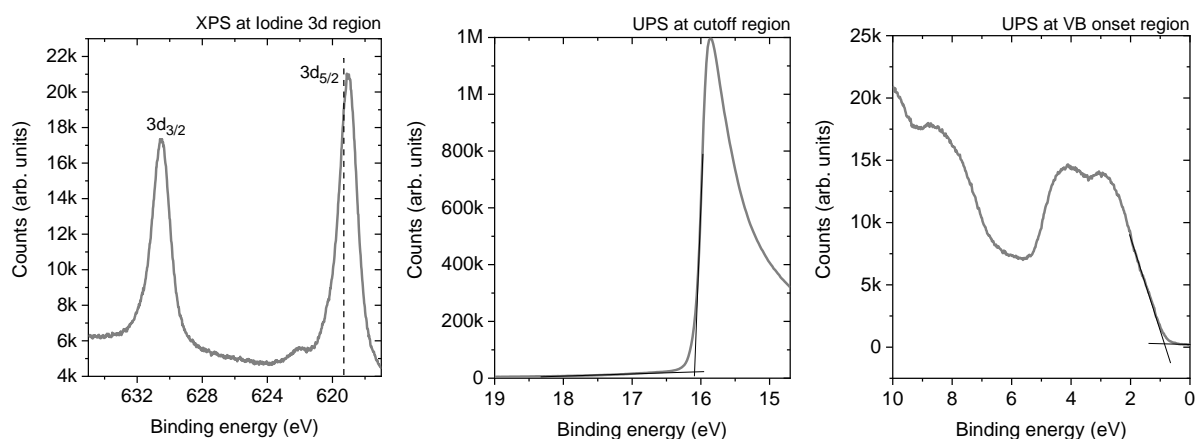


Figure S19 X-ray and UV Photoelectron spectroscopy of CsMAFA perovskite grown on PTAA (glass/ITO substrate). The dashed line in the XPS measurement (left) marks the expected position of the Iodine $3d_{5/2}$ peak¹⁹. The black lines in the UPS measurements (middle and right plot) are linear extrapolations of the leading edges.

Calculation of the dipole moment

The dipole moment was calculated following the previously published procedure²⁰. In brief, as the hole-selective fragment is electronically decoupled from the phosphonic acid group due to the non-conjugated linking ethylene fragment, the contribution of the PA fragment to the final dipole moment can be excluded (following the assumption that the binding to the ITO surface is roughly the same for all three SAMs). Therefore, for the calculations the phosphonic acid group was replaced by hydrogen. DFT calculations were performed using TURBOMOLE version 7.0 software²¹, with Becke's three parameter functional, B3LYP^{22,23}, and def2-SVP^{24,25} basis set in vacuum. Note that the mentioned dipole moments do not necessarily contribute in the relative same magnitude for all different SAMs, since the orientation relative to the ITO surface is not known for the individual SAMs.

8. Further PL measurements

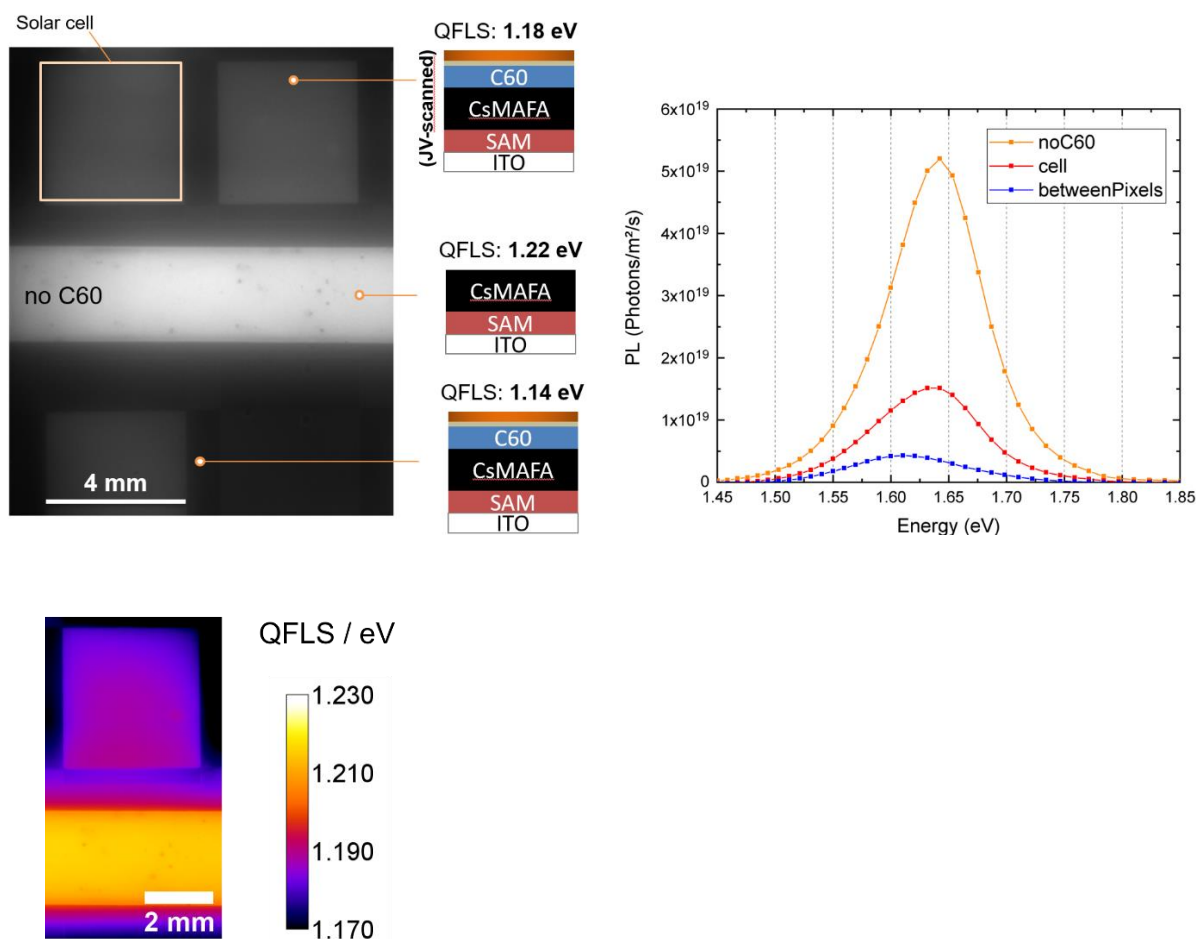


Figure S20 Absolute photoluminescence imaging of a sample with solar cells (bright squares, champion 2PACz device of the main text), recorded under an equivalent 1-sun intense fluence. By recording the photon-count calibrated PL spectra (displayed on the right for this sample) and applying the high-energy tail slope method as previously described for the same setup on perovskites,⁸ the quasi fermi-level splitting (QFLS) values are obtained. The solar cell pixel shows a QFLS of 1.18 eV, while the same solar cell shows 1.188 V V_{OC} in the J - V scan. The bright stripe in the middle of the image shows an area without C60 evaporated on the perovskite. The QFLS of 1.22 eV (PL quantum yield of $\sim 0.4\%$) represents the maximum possible V_{OC} with this perovskite on 2PACz and the comparison to the solar cell shows that the C60 interface is leading to a loss of ~ 40 meV. This, interestingly, is lower than for the same perovskite grown on PTAA.⁸ The lower panel shows a 2D plot of the QFLS of the upper part of the upper image (calculated from the difference of PL quantum yield to radiative limit²⁶, with same results as obtained with the high-energy tail slope fit).

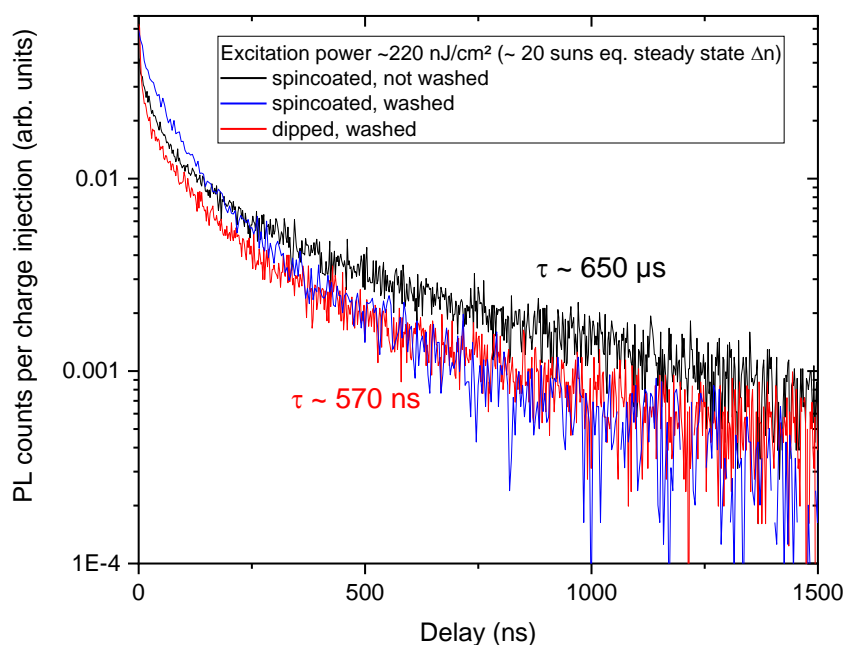


Figure S21 TrPL transients of CsMAFA perovskite film to investigate possible differences between spin-coating and dip-coating of the SAM solution (exemplary for MeO-2PACz). The non-significant difference is in line with the initially presented conclusions made with the RARS analysis.

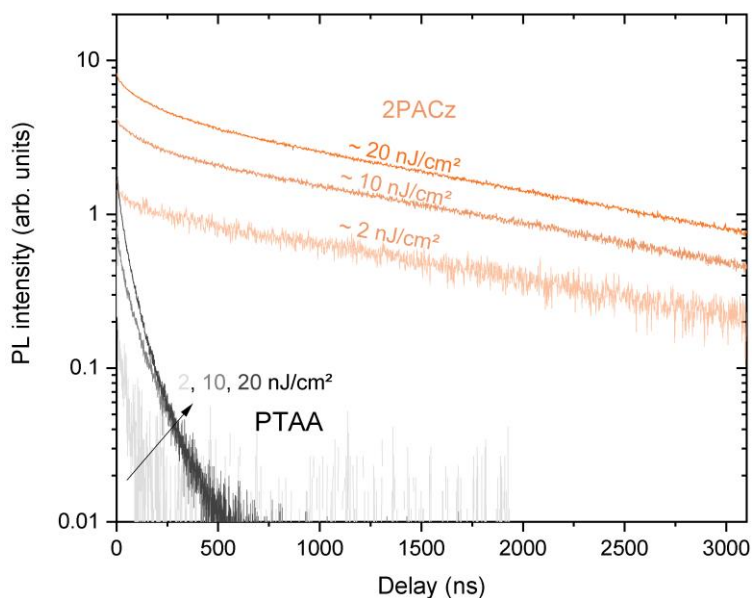


Figure S22a TrPL transients of CsMAFA perovskite films on 2PACz and PTAA for different excitation intensities.

Estimation of the interface recombination velocity

Assuming one-sided surface recombination (thus over-estimating S , since the CsMAFA top side is not passivated), we calculate the interface recombination velocity S through

$$\tau_2/2 = \frac{d}{S} + \frac{4}{D} \left(\frac{d^2}{\pi^2} \right),$$

with sample thickness d (~ 500 nm) and diffusivity D (~ 0.5). The calculated values for CsMAFA perovskite on the different HSCs are listed in the following table. Here, the two lifetimes were obtained from a bi-exponential fit, τ_2 corresponds to the value reported in the main text (which is roughly the same as obtained from a linear fit of the long tail), τ_1 was not used for the calculation:

	τ_1 (ns)	$\tau_2/2$ (ns)	S (cm/s)
Quartz glass	0	708	35
V1036	60	130	193
PTAA	60	200	125
MeO-2PACz	109	641	39
2PACz	161	2041	12

9. Certification Results

Seite 3/6
Page



10001090HMI059



Die Rückführung der Spektralmessung auf SI-Einheiten erfolgte über den Vergleich mit einer Standardlampe.
The traceability of the measurement of the spectral distribution to SI-Units is achieved using a standard lamp for the calibration of the spectroradiometer.

Identitäts-Nr. / Identity-Nr. :	Kalibrierschein-Nr./ Certificate-Nr. :	Rückführung/ Traceability :
BN-9101-451	40002-14-PTB	PTB

3. Messbedingungen

Measurement conditions

Standardtestbedingungen (STC) / Standard Testing Conditions (STC) :

Absolute Bestrahlungsstärke /
Total irradiance : 1000 W/m²

Temperatur des Messobjektes /
Temperature of the DUT : 25 °C

Spektrale Bestrahlungsstärke /
Spectral irradiance distribution : AM1.5G Ed.2 (2008)

Die Messung der IV-Kennlinie (Strom-Spannungs-Kennlinie) des Messobjektes erfolgt mit Hilfe eines Vierquadranten-Netztes und eines Kalibrierwiderstandes.

The measurement of the IV-curve is performed with a 4-quadrant power amplifier and a calibration resistor.

4. Messergebnis

Measurement results

Fläche / Area (da)¹: = (0.108 ± 0.003) cm²

¹: (t) = total area, (ap) = aperture area, (da) = designated illumination area /7/

Kennlinienparameter des Messobjektes unter Standardtestbedingungen (STC) / IV-curve parameter under Standard Testing Conditions (STC) :

		Vorwärtsrichtung / forwards scan direction	Rückwärtsrichtung / reverse scan direction	MPP-Tracking / MPP-Tracking
V _{oc}	=	(1156.7 ± 7.8) mV	(1158.3 ± 7.8) mV	
I _{SC} (Ed.2 - 2008)	=	(2.34 ± 0.04) mA	(2.34 ± 0.04) mA	
I _{MPP}	=	2.19 mA	2.18 mA	(2.20 ± 0.07) mA
V _{MPP}	=	999.6 mV	1004.3 mV	(1002.7 ± 24.2) mV
P _{MPP}	=	2.19 mW	2.19 mW	(2.21 ± 0.06) mW
FF	=	80.95 %	80.91 %	
η	=	20.29 %	20.28 %	(20.44 ± 0.82) %

Figure S23 Fraunhofer ISE certificate of a representative 2PACz solar cell with a CsMAFA perovskite absorber. The cell was masked from a 0.16 cm² area to ~ 0.108 cm² and then sent to the calibration laboratory.

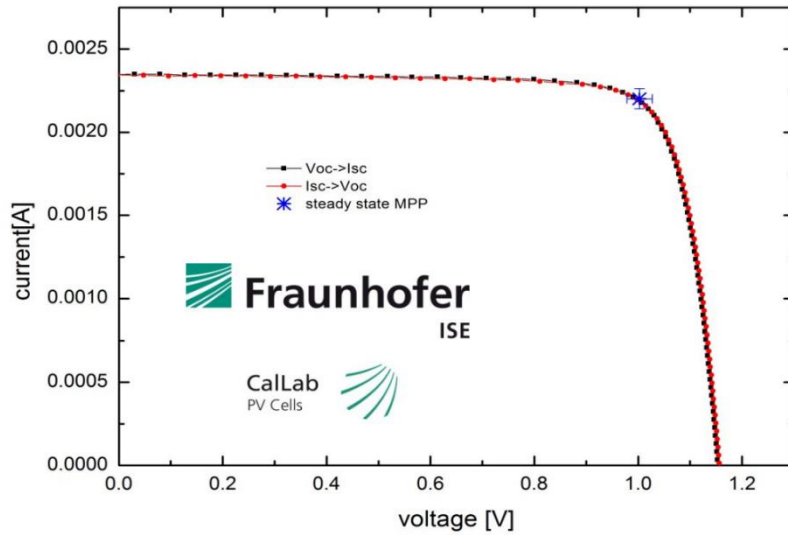


Figure S24 JV measurement by Fraunhofer ISE of a representative 2PACz solar cell with a CsMAFA perovskite absorber.

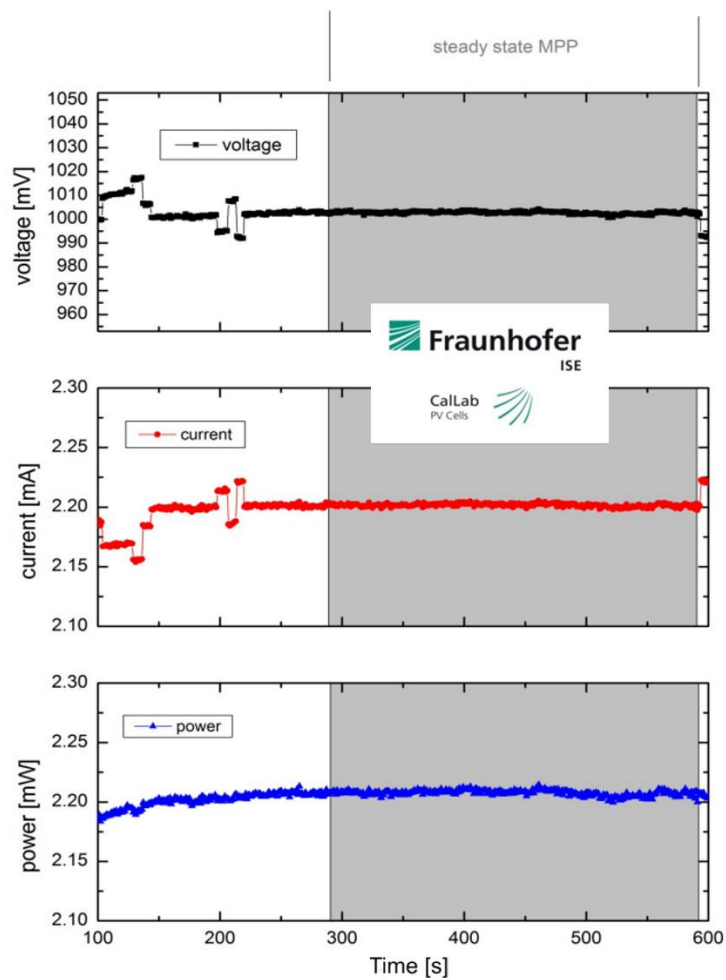


Figure S25 MPP tracking measurement by Fraunhofer ISE of a representative 2PACz solar cell with a CsMAFA perovskite absorber. The certified PCE value of 20.44 % is drawn from this measurement. The in-house MPP measurement of this device was 20.7 % 2 weeks prior to certification (with an in-house measured area of 0.107 cm², FF of 81.6% and V_{OC} of 1.15 V).

10. Additional results with the other perovskite absorbers

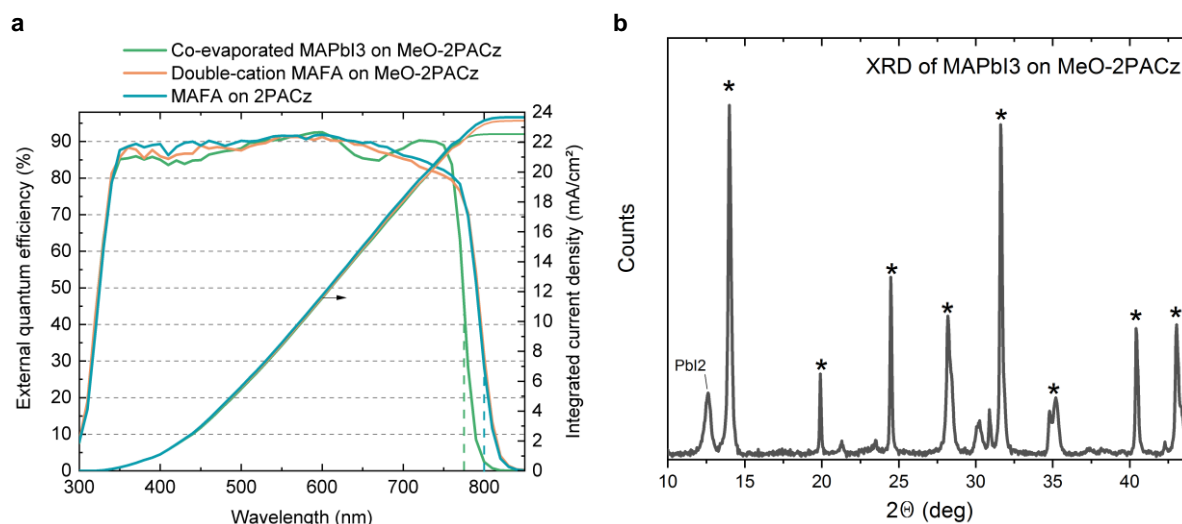


Figure S26 a, External quantum efficiency measurements of the “double” and “single” cation perovskite solar cells shown in fig. 7a of the main text, and corresponding integration of the product of EQE and AM1.5G spectrum (right axis). The JV-curve of the 2PACz/MAFA cell is shown in fig. S23. The vertical dashed lines indicated the position of the maximum of the curve’s derivative (for estimation of the optical band gap, 775 nm for MAPbI₃ and 800 nm for MAFA). **b**, XRD of a representative MAPbI₃ perovskite prepared by co-evaporation on MeO-2PACz. The asterisks indicate the expected perovskite crystal diffraction peaks.

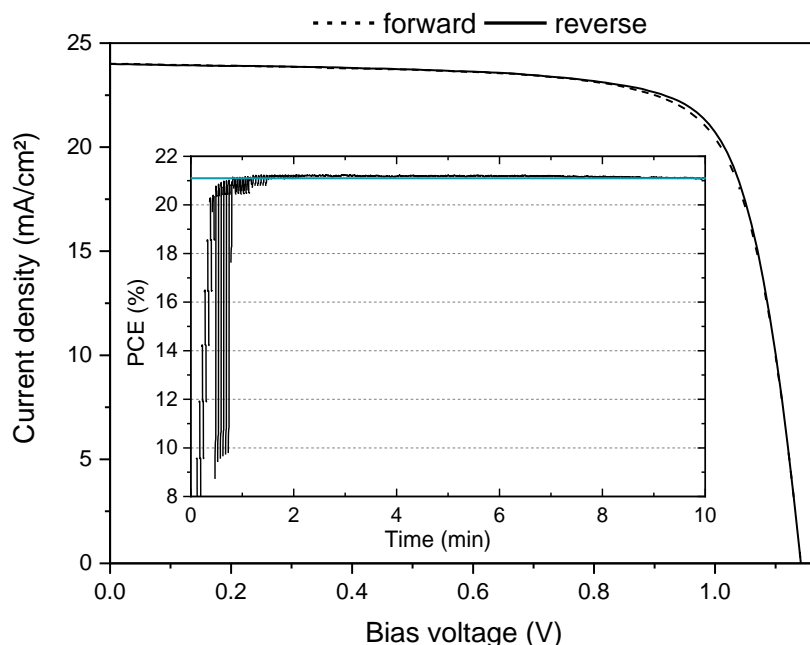


Figure S27 J-V scan (250 mV/s scan rate) at standard measurement conditions and MPP tracking in the inset of a PSC based on “double-cation” MAFA perovskite on 2PACz. Compared to MeO-2PACz, the V_{oc} is slightly higher, following the trend presented with CsMAFA in the main text. Device metrics are (reverse scan parameters): PCE = 21.0 %, V_{oc} = 1.142 V, FF = 76.7 %, J_{sc} = 24.0 mA/cm² (integrated EQE x AM1.5G = 23.7 mA/cm²). The blue line in the MPPT inset marks the 21.1 % value.

11. Additional results to the Perovskite/CIGSe Tandem

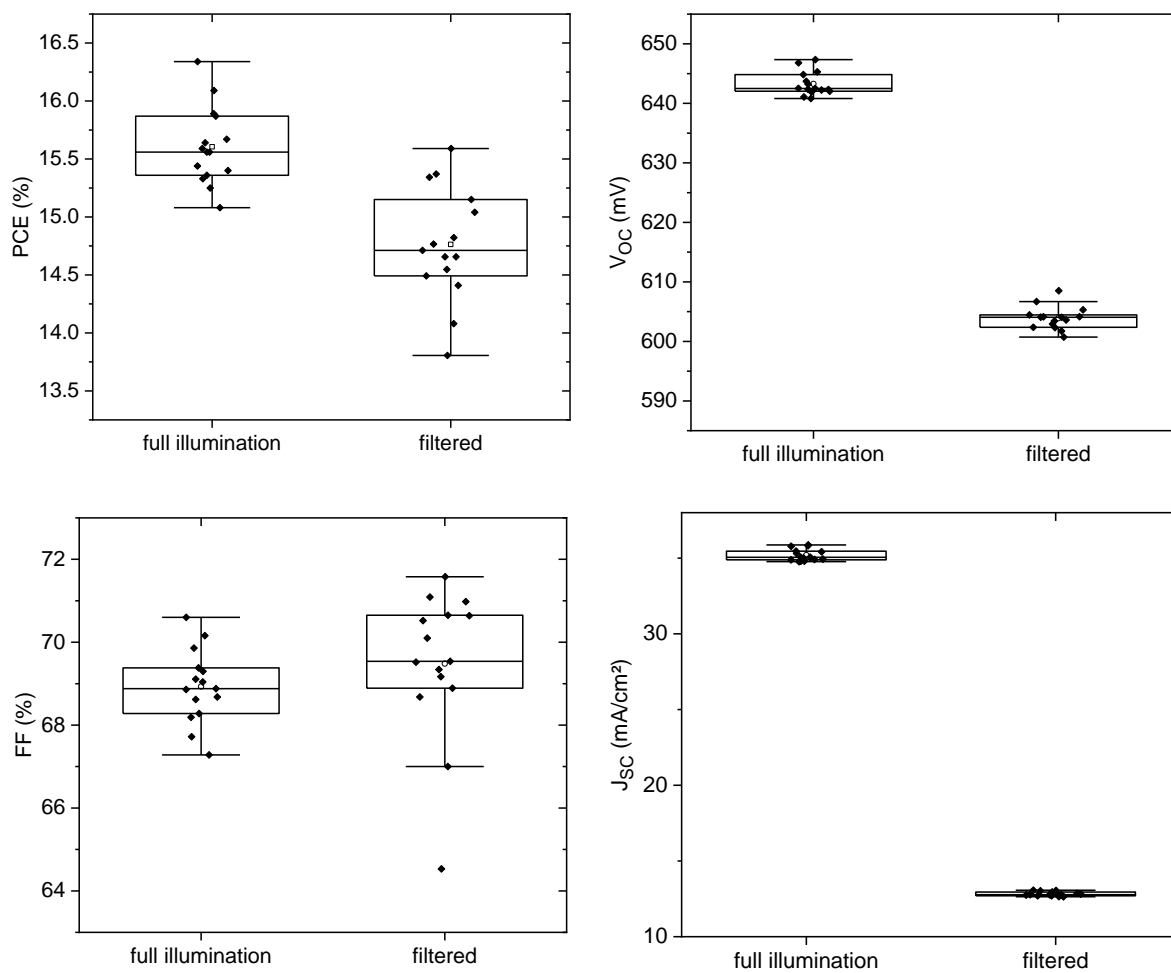


Figure S28 Solar cell device metrics of representative CIGSe bottom cells, similar to the one used for the tandem cell, under full 1-sun illumination and filtered for visible range absorption (as absorbed by the perovskite). The PCE values for the filtered case have been adjusted for the smaller illumination intensity.

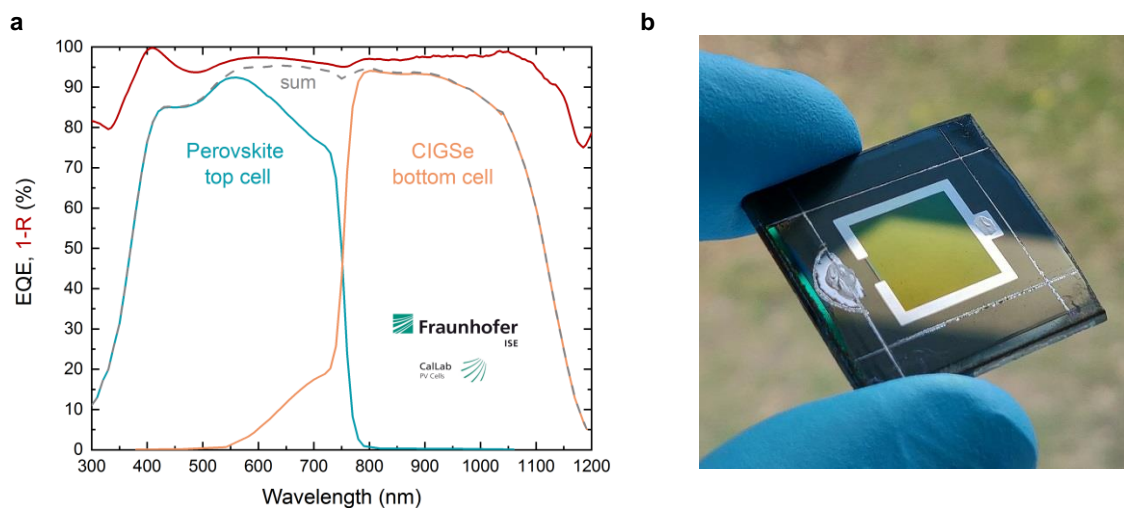


Figure S29 a, External quantum efficiency measurement (provided by Fraunhofer ISE, Callab) of the CIGSe/perovskite monolithic tandem solar cell shown in figure 6b of the main text. The red line shows a 1-reflection measurement of the certified cell measured in-house. **b**, photograph of a representative CIGSe/perovskite monolithic tandem solar cell with $\sim 1 \text{ cm}^2$ active area (surrounded by a silver frame).

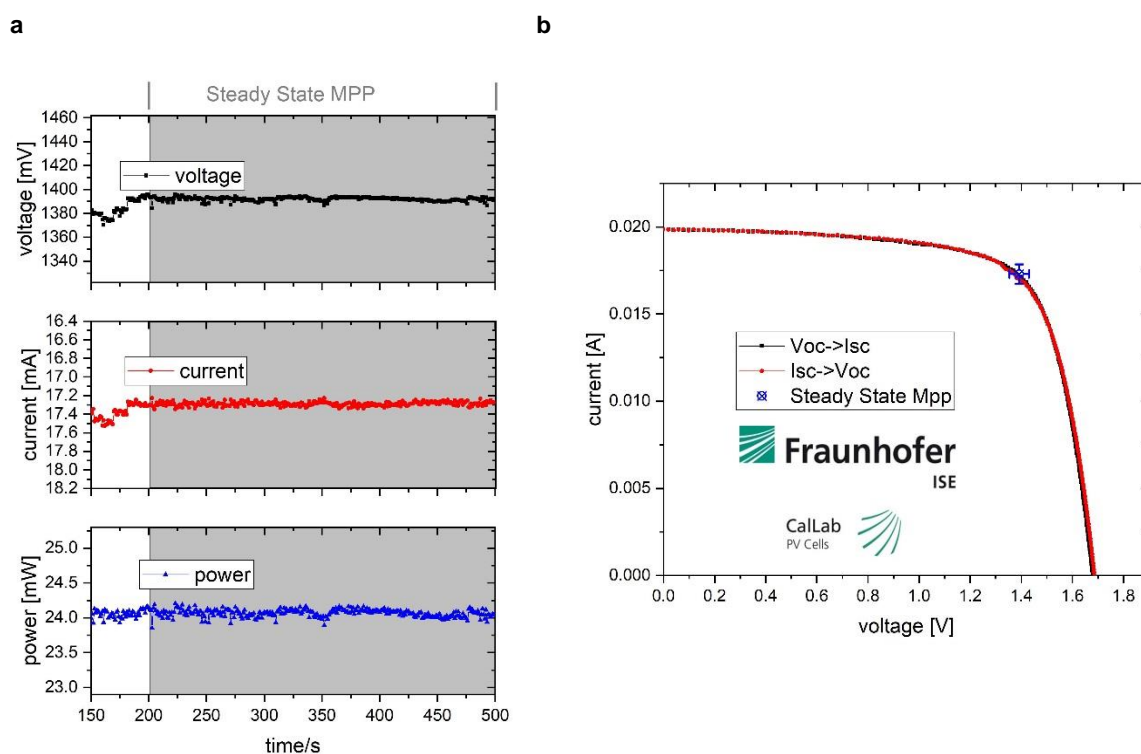


Figure S30 Certification results by Fraunhofer ISE of the CIGSe/Perovskite tandem solar cell (area $\sim 1.035 \text{ cm}^2$). **a**, maximum power point tracking from which the steady-state MPP value was extracted (in-house measurement was 23.2 %, fitting to the certified 23.26 %). **b**, J-V curve.

1. Beschreibung des Kalibriergegenstandes

Description of the calibrated object

Das Messobjekt ist eine Tandem-Solarzelle . Typ: Perowskit/CIGSe.

The device under test is a perovskite-CIGSe tandem solar cell.

2. Messverfahren

Measurement procedure

Die Kalibrierung des Kalibrierobjektes wird gemäß /1/ mit einem Zweilampen-DC-Sonnensimulator durchgeführt. Die Einstrahlung wird mit Hilfe einer Monitorzelle während der gesamten Messdauer aufgenommen und deren Schwankungen bezüglich der Messung korrigiert. Die Divergenz der Randstrahlen ist < 5°. Die Solarzelle wird auf einem Vakuumprobentisch thermisch stabilisiert.

The calibration of the test sample was performed at Standard Testing Conditions (STC) with a dual light steady-state solar simulator according to /1/. The irradiance is controlled with a monitor cell during the measurement in order to correct fluctuations. The divergence of the peripheral beams is < 5°. The solar cell is kept at a constant temperature

Rückführung der Referenzsolarzellen/Traceability of the reference solar cells :

Identitäts-Nr. / <i>Identity-Nr. :</i>	Kalibrierschein-Nr./ <i>Certificate-Nr. :</i>	Rückführung/ <i>Traceability :</i>
007-2012	47149-PTB-17	PTB
022-2018	47114-PTB-18	PTB

Die Korrektur der spektralen Fehlanpassung (Mismatch), die durch die Abweichung der spektralen Verteilung des Sonnen Simulators vom Standard-Spektrum AM1.5G /3/ in Kombination mit den verschiedenen spektralen Empfindlichkeiten von Referenzzelle und Messobjekt entsteht /4/, wurde durch eine erweiterte Mismatchberechnung /4/ - wie in /2/ beschrieben - korrigiert.

Dazu wurde die spektrale Verteilung der Bestrahlung (Sonnensimulator) mit einem Spektralradiometer und die spektrale Empfindlichkeit des Messobjektes mit einem laserbasierten Messplatz /5/ gemessen (s. Kalibrierschein Nr: 9005085HMI0418).

The spectral mismatch - caused by the deviation of the simulator spectrum from the standard spectrum AM1.5G /3/ in combination with the difference between the spectral response of the reference cell and that of the device under test (DUT) – is calculated by a generalized mismatch correction /3/ as described in /2/.

For the spectral mismatch correction the spectral distribution of the solar simulator is measured with a spectroradiometer, the spectral response of the DUT is measured with a laser-based setup according to /5/ (cf.

Der P_{MPP} wurde durch MPP-Tracking über 500s bestimmt. Der angegebene P_{MPP} ist der Mittelwert der letzten 300s dieser stabilisierten Messung. Anschließend wurde die IV-Kennlinie in zwei Richtungen ($V_{OC} \rightarrow I_{SC}$ und $I_{SC} \rightarrow V_{OC}$) aufgenommen.

The P_{MPP} was determined by MPP-Tracking for 500s. The reported P_{MPP} represents the average value of the last 300s of this stabilized measurement. Afterwards, the IV-curve was determined with a scan in both directions ($V_{OC} \rightarrow I_{SC}$ and $I_{SC} \rightarrow V_{OC}$).

Figure S31 Certification sheet for the CIGSe/perovskite tandem, description of the measurement procedure and type of solar cell.

Supporting Information References

- 1 A. Magomedov, A. Al-Ashouri, E. Kasparavičius, S. Strazdaite, G. Niaura, M. Jošt, T. Malinauskas, S. Albrecht and V. Getautis, *Adv. Energy Mater.*, 2018, **8**, 1801892.
- 2 P. Zhao, B. J. Kim, X. Ren, D. G. Lee, G. J. Bang, J. B. Jeon, W. Bin Kim and H. S. Jung, *Adv. Mater.*, 2018, **1802763**, 1–8.
- 3 M. Jošt, T. Bertram, D. Koushik, J. A. Marquez, M. A. Verheijen, M. D. Heinemann, E. Köhnen, A. Al-Ashouri, S. Braunger, F. Lang, B. Rech, T. Unold, M. Creatore, I. Lauer mann, C. A. Kaufmann, R. Schlatmann and S. Albrecht, *ACS Energy Lett.*, 2019, **4**, 583–590.
- 4 E. Köhnen, M. Jošt, A. B. Morales-Vilches, P. Tockhorn, A. Al-Ashouri, B. Macco, L. Kegelm ann, L. Korte, B. Rech, R. Schlatmann, B. Stannowski and S. Albrecht, *Sustain. Energy Fuels*, , DOI:10.1039/c9se00120d.
- 5 M. Talaikis, O. Eicher-Lorka, G. Valincius and G. Niaura, *J. Phys. Chem. C*, 2016, **120**, 22489–22499.
- 6 V. Shrotriya, G. Li, Y. Yao, T. Moriarty, K. Emery and Y. Yang, *Adv. Funct. Mater.*, 2006, **16**, 2016–2023.
- 7 M. Wojdyr, *J. Appl. Crystallogr.*, 2010, **43**, 1126–1128.
- 8 M. Stolterfoht, C. M. Wolff, J. A. Márquez, S. Zhang, C. J. Hages, D. Rothhardt, S. Albrecht, P. L. Burn, P. Meredith, T. Unold and D. Neher, *Nat. Energy*, 2018, **3**, 847–854.
- 9 A. Delamarre, L. Lombez and J. F. Guillemoles, *Appl. Phys. Lett.*, 2012, **100**, 2012–2015.
- 10 S. A. Paniagua, P. J. Hotchkiss, S. C. Jones, S. R. Marder, A. Mudalige, F. S. Marrikar, J. E. Pemberton and N. R. Armstrong, *J. Phys. Chem. C*, 2008, **112**, 7809–7817.
- 11 M. Bomers, A. Mezy, L. Cerutti, F. Barho, F. Gonzalez-Posada Flores, E. Tournié and T. Taliercio, *Appl. Surf. Sci.*, 2018, **451**, 241–249.
- 12 W. Zhang, W. Ju, X. Wu, Y. Wang, Q. Wang, H. Zhou, S. Wang and C. Hu, *Appl. Surf. Sci.*, 2016, **367**, 542–551.
- 13 R. Quiñones, S. Garretson, G. Behnke, J. W. Fagan, K. T. Mueller, S. Agarwal and R. K. Gupta, *Thin Solid Films*, 2017, 642, 195–206.
- 14 J. A. Guerra, A. Tejada, L. Korte, L. Kegelm ann, J. A. Töfflinger, S. Albrecht, B. Rech and R. Weingärtner, *J. Appl. Phys.*, 2017, **121**, 173104.
- 15 J. S. Kim, P. K. H. Ho, D. S. Thomas, R. H. Friend, F. Cacialli, G. W. Bao and S. F. Y. Li, *Chem. Phys. Lett.*, 1999, **315**, 307–312.
- 16 C. Donley, D. Dunphy, D. Paine, C. Carter, K. Nebesny, P. Lee, D. Alloway and N. R. Armstrong, *Langmuir*, 2002, **18**, 450–457.
- 17 A. W. C. Lin, N. R. Armstrong and T. Kuwana, *Anal. Chem.*, 1977, **49**, 1228–1235.
- 18 P. J. Hotchkiss, S. C. Jones, S. A. Paniagua, A. Sharma, B. Kippelen, N. R. Armstrong and S. R. Marder, *Acc. Chem. Res.*, 2012, **45**, 337–346.
- 19 J. F. Moulder, W. F. Stickle, P. E. Sobol and K. D. Bomben, *Handbook of X-ray Photoelectron Spectroscopy*, 1992.
- 20 I. Lange, S. Reiter, M. Pätz el, A. Zykov, A. Nefedov, J. Hildebrandt, S. Hecht, S. Kowarik, C. Wöll, G. Heimel and D. Neher, *Adv. Funct. Mater.*, 2014, **24**, 7014–7024.
- 21 R. Ahlrichs, M. Bär, M. Häser, H. Horn and C. Kölmel, *Chem. Phys. Lett.*, 1989, **162**, 165–169.
- 22 C. Lee, W. Yang and R. G. Parr, *Phys. Rev. B*, 1988, **37**, 785–789.
- 23 A. D. Becke, *J. Chem. Phys.*, 1993, **98**, 5648–5652.
- 24 A. Schäfer, H. Horn and R. Ahlrichs, *J. Chem. Phys.*, 1992, **97**, 2571–2577.
- 25 F. Weigend and R. Ahlrichs, 2005, 3297–3305.
- 26 R. T. Ross, *J. Chem. Phys.*, 1967, **46**, 4590–4593.